4th Flow Control Conference
23 - 26 June 2008, Seattle, Washington

AIAA 2008-4085

Large-Eddy Simulations of Zero-Net-Mass-Flux Jet Based Separation Control in a Canonical Separated Flow

Rupesh B. Kotapati * and Rajat Mittal †

Department of Mechanical and Aerospace Engineering

The George Washington University, Washington, DC 20052, USA

Frank Ham ‡

Center for Turbulence Research

Stanford University, Stanford, CA 94305, USA

Large-eddy simulations (LES) are used to study the effects of three-dimensionality on synthetic-jet forcing of a separated flow in a configuration previously devised by Mittal *et al*[1] for investigating active separation control using zero-net-mass-flux jets. Large-eddy simulations of the baseline separated flow show that the boundary layer separates earlier and the separated shear layer rolls up farther away in three-dimensional simulations than in two-dimensional (2-D) direct simulations. However, similar to two-dimensional simulations, LES of the baseline separated flow indicates that the entire system, comprised of the shear layer, separation zone and wake, locks on to a single frequency. Zero-net-mass-flux forcing of the separated flow at the superharmonics of this baseline lock-on frequency results in two-dimensionalization of the bulk flow yielding similar spectral dynamics and lock-on states as the 2-D simulations. In particular, most effective separation control is found to occur at the first superharmonic of the baseline lock-on frequency for which the shear layer, the separated region and the wake lock on to the fundamental forcing frequency. The existence of such a harmonic lock-on state due to forcing is found to be associated with a more regularized flow than the non-resonant case, thereby resulting in effective separation control.

Nomenclature

C_μ	ZNMF jet momentum coefficient, $C_\mu = 2(d/c)(V_J/U_\infty)^2$.
C_f	Mean skin-friction coefficient, $C_f = 2\tau_w/(\rho U_\infty^2)$.
C_p	Pressure coefficient, $C_p = (p - p_\infty)/q_\infty$.
E_{vv}	One-dimensional energy spectrum of v.
H	Height of the ZNMF actuator cavity.
L_x, L_y, L_z	Computational domain sizes in x, y, and z directions, respectively.
N_x, N_y, N_z	Number of grid cells in x, y, and z directions, respectively.
W	Width of the ZNMF actuator cavity.
X_{TE}	Distance between the separation location and the trailing edge.
F_J^+	Non-dimensional forcing frequency, $F^+ = f_J c/U_\infty$.
H_{sep}	Height of the separation bubble.
L_{sep}	Length of the separation bubble.
Re_c	Reynolds number based on free-stream velocity and chord length, $Re_c = U_\infty c/\nu$.
U_∞	Free-stream velocity.

*Currently CFD Physics Validation Engineer, Exa Corporation; rupesh@exa.com, Member AIAA.
†Professor; mittal@gwu.edu, Associate Fellow AIAA.
‡Engineering Research Associate; fham@stanford.edu.

V_J Characteristic velocity of the ZNMF jet.
f_J Forcing frequency of the ZNMF jet "device".
f_{sep} Separation bubble frequency.
f_{SL} Shear layer frequency.
f_{wake} Wake vortex shedding frequency.
c Airfoil chord.
d Width of the ZNMF jet slot.
h Height of the ZNMF actuator slot.
p Pressure.
q_∞ Free-stream dynamic pressure, $q_\infty = (1/2)\rho U_\infty^2$.
t Time.
u, v, w Streamwise, cross-stream and spanwise velocity components, respectively.
u_i General notation for velocity components: $u_1 \equiv u$, $u_2 \equiv v$.
$v^e(x,t)$ y-component of the velocity at the exit plane of the ZNMF jet orifice.
x_J Streamwise location of ZNMF forcing.
x_i General notation for spatial coordinates: $x_1 \equiv x$, $x_2 \equiv y$, $x_3 \equiv z$.
x_{sep} Streamwise location of primary separation.

Subscripts

i Directional index, $i = 1, 2, 3$.

Conventions

$|\cdot|$ Magnitude of a tensor quantity, e.g. $|S| = \sqrt{2S_{ij}S_{ij}}$
$\underline{\langle\cdot\rangle}$ Time-averaged quantity
$\overline{(\cdot)}$ Grid-filtered quantity
$\widehat{(\cdot)}$ Test-filtered quantity; Complex Fourier coefficient; An intermediate time level in fractional-step method

Symbols

ν Kinematic viscosity.
$\omega_x, \omega_y, \omega_x$ Vorticity components in x, y, z directions, respectively.
ρ Density.
τ_w Wall shear stress.

Superscripts

$*$ Dimensionless variable.
0 Baseline flow conditions.

I. Introduction

A novel numerical configuration was earlier proposed by Mittal *et al*[1] for investigating zero-net-mass-flux (ZNMF) or synthetic jet based separation control in canonical separated airfoil flows. Using this configuration, a separation bubble of prescribed size can be created at a desired location on the upper surface of a flat-plate airfoil at zero-incidence by imposing an adverse pressure gradient through blowing and suction on the top boundary of the computational domain. Mittal *et al.*[1] carried out two-dimensional simulations of this flow configuration with separation induced at different streamwise stations to show that these canonical separated flows are characterized by at least three distinct frequency scales corresponding to the shear layer instability f_{SL}, the unsteadiness of the separated region f_{sep} and the vortex shedding in the wake f_{wake}. The resonant interaction between these different scales is generally dependent on the distance between the separation zone and the trailing edge. Kotapati *et al.*[2] investigated the dynamics of mid-chord separation and its control at a chord-based Reynolds number Re_c of 6×10^4. They used two-dimensional simulations to study the effect of varying the actuation frequency, duty cycle and actuator location on separation control. Kotapati *et al.*[3] further extended this work by investigating the dynamics and control of aft-chord separation in the vicinity of vortex shedding in the wake. Their studies indicated that the entire system, comprising the shear layer, the separated region and the wake, locks on to a single frequency and that forcing the shear

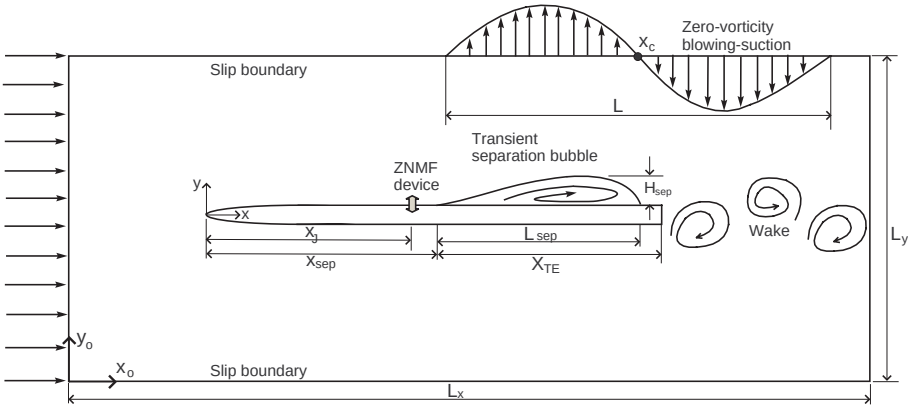

Figure 1. Schematic of the flow configuration (not to scale).

layer close to this lock-on frequency or its first superharmonic yields effective control of the mean separation bubble.

It has been well acknowledged by the CFD community that two-dimensional (2-D) numerical simulations of intrinsically three-dimensional flows, even below critical Reynolds numbers, over nominally two-dimensional bluff bodies lead to inaccurate prediction of aerodynamic forces, whereas three-dimensional (3-D) simulations lead to accurate predictions. Even though the airfoil geometry employed in the previous studies was not a bluff body and the objective of the numerical experiments was separation control rather than direct enhancement of the lift-to-drag ratio, it would still be useful to investigate the effect of spanwise instability mechanisms on the scaling of the characteristic frequencies of the separated system and its subsequent control. To this end, large-eddy simulations (LES) of the flow configuration with aft-chord separation are carried out at $Re_c = 6 \times 10^4$ to assess the effect of three-dimensionality on the scaling of characteristic frequencies of the separated system and its subsequent control.

II. Flow Configuration

Figure 1 shows a schematic of the flow configuration used in the simulations. It consists of a 5% thick, spanwise homogeneous, flat-plate airfoil of chord c with 8:1 elliptic leading edge and blunt trailing edge at 0° angle-of-attack in a free-stream. The blunt trailing edge is chosen to fix the separation point of the lower- and upper-side shear layers at the sharp corners of the trailing face, and provide an unambiguous definition for the characteristic width of the wake. The origin of the global coordinate system (x_0, y_0, z_0) is fixed at the lower left-hand corner in the mid-span of the computational domain that measures L_x, L_y and L_z in x_0, y_0 and z_0 directions, respectively. The origin of the local coordinate system (x, y, z) is at the leading edge of the airfoil in the same mid-span plane. Note that x, y and z are in the streamwise, cross-stream and spanwise directions, respectively.

A separation bubble of desired size can be induced at any location on the upper surface of the flat plate by applying an adverse pressure gradient through suction and blowing on the upper boundary of the computational domain. The technique of Na & Moin[4] is adopted wherein a zero-vorticity boundary condition of the following form is prescribed on the upper boundary:

$$v(x_0, L_y) = G(x_0), \qquad \left.\frac{\partial u}{\partial y_0}\right|_{(x_0, L_y)} = \frac{\mathrm{d}G}{\mathrm{d}x_0}, \tag{1}$$

where $G(x_0)$ is the prescribed steady suction and blowing velocity profile, and the Neumann boundary condition on u ensures that no spanwise vorticity (ω_z) is generated due to suction and blowing. In this study, $G(x_0)$ is of the form:

$$G(x_0) = -V_{top} \sin\left(\frac{2\pi(x_0 - x_c)}{L}\right) \mathrm{e}^{-\alpha\left(\frac{2(x_0 - x_c)}{L}\right)^{\beta}}, \tag{2}$$

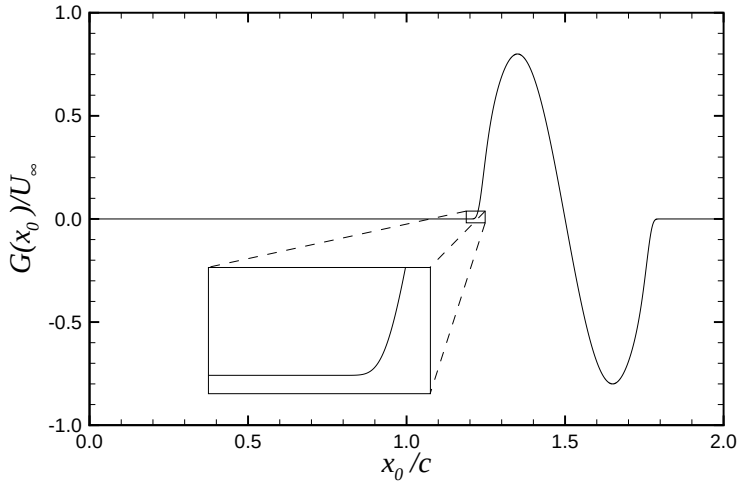

Figure 2. Plot of function $G(x_0)$ for the case of aft-chord separation induced by prescribing suction and blowing over $1.2 \leq x_0/c \leq 1.8$ on the top boundary of the computational domain.

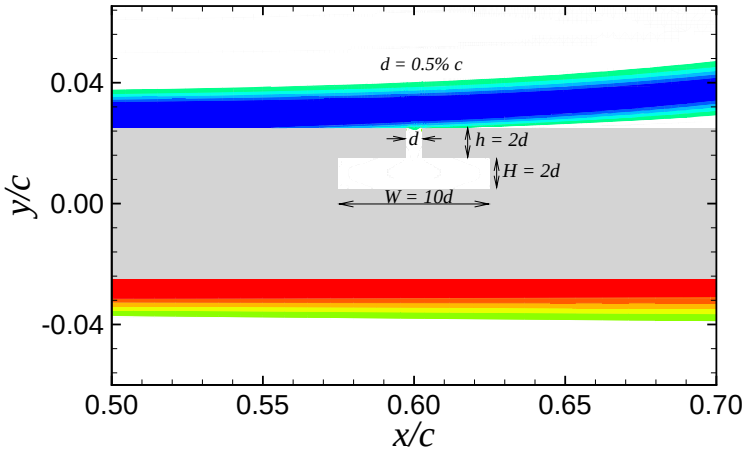

Figure 3. Schematic of the ZNMF actuator embedded in the airfoil. The contours of spanwise vorticity show attached and separated boundary layers on the lower and upper surfaces of the airfoil, respectively.

where x_c is the center of the steady suction and blowing velocity profile in the global system and L is the length of the profile (see figure 1). The function $G(x_0)$ allows independent prescription of the location as well as the streamwise size of the separation region by varying x_c and L. In equation 2, the sinusoidal function that models the suction and blowing profile is multiplied by an exponential blending function to provide continuity at the edges of the profile as it transitions to slip boundary condition on either side. The parameters V_{top}, α and β are set to $0.8U_\infty$, 10 and 20, respectively. Figure 2 shows the plot of function $G(x_0)$ for the case of aft-chord separation induced by prescribing suction and blowing over $1.2 \leq x_0/c \leq 1.8$ on the top boundary of the computational domain. Thus, separation can be produced anywhere on the plate surface and the above configuration can be used to examine the nonlinear interactions between the shear layer, separation region, and airfoil wake in controlled as well as uncontrolled versions of these flows. It should be noted that with this configuration, the confounding effect of curvature is eliminated, something that is usually not possible with conventional airfoil geometries.

Rather than simply model the ZNMF jet by prescribing a localized analytical velocity profile on the flat plate, the flow inside the ZNMF actuator and the resulting synthetic jet are simulated in the current study. This is done by embedding a slot and cavity under the upper surface of the flat plate as shown in figure 3. The ZNMF 'device' consists of a reactangular slot, of width $d = 0.005c$ and height $h = 2d$, connected to an internal rectangular cavity of width $W = 10d$ and height $H = 2d$. The choice of these dimensions for the

ZNMF 'device' is driven by the design of a ZNMF actuator used by Schaeffler *et al.*[5] in the NASA LaRC 2004 workshop on CFD validation of synthetic jets and turbulent separation control. In the experiments, the ZNMF jet through the slot is usually generated by the motion of a piston or a piezoelectric diaphragm mounted to the sides or the bottom of the cavity. In the computations, a simple oscillatory velocity boundary condition of the form $[u, v] = [0, V_0 \sin(2\pi f_J t)]$ is prescribed at the lower horizontal boundary of the cavity, where V_0 is the velocity amplitude and f_J is the oscillation frequency. This boundary condition essentially provides a simple sinusoidal representation of the mass flux produced in the slot by the motion of the piston or diaphragm in the experiments.

The characteristic velocity of the ZNMF jet is given by

$$V_J = \frac{2}{AT} \int_0^{T/2} \int_A v^e(x,t)\, \mathrm{d}A\, \mathrm{d}t, \tag{3}$$

where $v^e(x,t)$ is the y component of the velocity at the exit plane of the orifice, A is the cross-sectional area of the orifice, and $T = 1/f_J$ is the time period of the synthetic jet cycle. In the current incompressible simulations, the velocity amplitude at the lower boundary of the cavity V_0 is related to the characteristic jet velocity V_J through mass conservation by $V_0 = (\pi V_J/2)(d/W)$. Thus, V_J can be prescribed by applying a suitable value of V_0.

III. Governing Equations

The flow field over the proposed canonical configuration is modeled by unsteady incompressible Navier–Stokes equations, written in non-dimensional tensor form as

$$\frac{\partial u_i^*}{\partial x_i^*} = 0, \tag{4}$$

$$\frac{\partial u_i^*}{\partial t^*} + \frac{\partial u_i^* u_j^*}{\partial x_j^*} = -\frac{\partial p^*}{\partial x_i^*} + \frac{1}{Re} \frac{\partial^2 u_i^*}{\partial x_j^* \partial x_j^*}, \tag{5}$$

where x_i^* are the Cartesian coordinates, t^* is the time, p^* is the pressure, and u_i^* are the Cartesian velocity components. All the coordinate variables, time, velocity components, and pressure are non-dimensionalized by chord length c, convective time scale c/U_∞, inflow free-stream velocity U_∞, and ρU_∞^2, respectively. The Reynolds number is defined as $Re = U_\infty c/\nu$. For the sake of brevity, the superscript $*$ denoting nondimensional variables in the above equations will be dropped in the remainder of this section.

In LES methodolgy, the Navier–Stokes equations are spatially filtered, the energy-carrying large scales are explicitly resolved, and the influence of more universal and homogeneous subgrid scales (SGS) on the resolved scales is modeled or parameterized using closures of various degrees of complexity. When the Navier–Stokes equations are spatially filtered (denoted by the overbar) using a filter that commutes with the spatial and temporal derivatives, one obtains the following LES equations:

$$\frac{\partial \bar{u}_i}{\partial x_i} = 0 \tag{6}$$

$$\frac{\partial \bar{u}_i}{\partial t} + \frac{\partial \bar{u}_i \bar{u}_j}{\partial x_j} = -\frac{\partial \bar{p}}{\partial x_i} - \frac{\partial \tau_{ij}}{\partial x_j} + \frac{1}{Re} \frac{\partial^2 \bar{u}_i}{\partial x_j \partial x_j}, \tag{7}$$

where $\tau_{ij} = \overline{u_i u_j} - \bar{u}_i \bar{u}_j$ is the subgrid-scale (SGS) stress tensor that must be modeled.

The SGS stress tensor is parameterized by the dynamic Smagorinsky model (Germano *et al.*[6]):

$$\tau_{ij} - \frac{\delta_{ij}}{3}\tau_{kk} = -2\nu_T \overline{S}_{ij} = -2C\overline{\Delta}^2 |\overline{S}| \overline{S}_{ij} \tag{8}$$

where δ_{ij} is the Kronecker delta ($\delta_{ij} = 1$, if $i = j$; $\delta_{ij} = 0$, if $i \neq j$), $\overline{\Delta}$ denotes the grid-filter width, $\overline{S}_{ij} = (\partial \bar{u}_i/\partial x_j + \partial \bar{u}_j/\partial x_i)/2$ denotes the filtered strain-rate tensor, and $|\overline{S}| = (2\overline{S}_{ij}\overline{S}_{ij})^{1/2}$ is the magnitude of the strain-rate tensor. The model coefficient C is computed dynamically using the least-squares approach proposed by Lilly[7] :

$$C = -\frac{1}{2} \frac{\langle L_{ij} M_{ij} \rangle}{\langle M_{kl} M_{kl} \rangle} \tag{9}$$

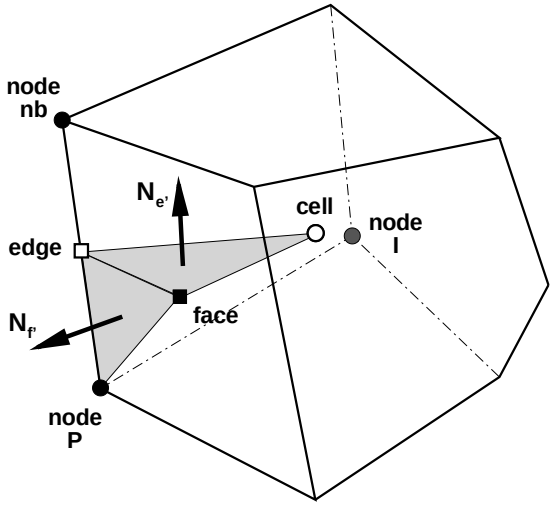

Figure 4. Schematic of the three-dimensional node-based unstructured mesh (adapted from Ham *et al.*[10]

where

$$L_{ij} = \widehat{\overline{u}_i \overline{u}_j} - \widehat{\overline{u}}_i \widehat{\overline{u}}_j \tag{10}$$

and

$$M_{ij} = -\bar{\Delta}^2 |\bar{S}| \bar{S}_{ij} + \widehat{\Delta}^2 |\widehat{\bar{S}}| \widehat{\bar{S}}_{ij}. \tag{11}$$

The above dynamic procedure requires the application of a test filter of characteristic width $\widehat{\Delta}$, signified by a caret ($\widehat{\ }$) over the overbar, to the filtered Navier–Stokes equations. The ratio of test filter to grid filter widths is set to be $\widehat{\Delta}/\overline{\Delta} = 2$ as was found to be optimal by Germano *et al.*[6] The grid-filter width is defined as $V^{1/3}$ where V denotes the volume of the grid cell. In equation 9, the angular brackets denote local averaging in space.

A. Numerical algorithm

Upwind-biased numerical schemes that make the solution procedures robust over a wide range of Reynolds numbers by providing numerical dissipation to control aliasing errors are not suitable for high-fidelity methods like DNS and LES. Mittal & Moin[8] have shown that upwind-biased schemes adversely affect the acuracy of the LES predictions since the numerical dissipation produced in the coarse-grid regions often overwhelms the contributions of the SGS model and molecular viscosity, besides depriving the solution of the proper Reynolds number sensitivity. An alternative to achieving robustness is to develop non-dissipative numerical schemes that control aliasing errors by enforcing discrete conservation of kinetic energy in addition to conservation of mass and momentum. Discrete energy conservation in incompressible flows refers to the fact that the convective and pressure terms in the discrete energy equation are expressible in divergence form (i.e. solely in terms of contributions from the flow boundaries).

The flow field is computed using CDP[a], an unstructured grid finite-volume-based flow solver being actively developed at Stanford University's Center for Integrated Turbulence Simulations (CITS) as part of the U.S. Department of Energy's (DOE's) Advanced Simulation and Computing (ASC) program. The solver uses a non-staggered formulation on hybrid unstructured grids that eliminates the shortcomings of extending the discrete energy-conserving algorithm of Harlow & Welch[9] for structured grids to unstructured grids. Figure 4 illustrates the location of primitive variables in this formulation. The full Cartesian velocity vector u_i and pressure p are located at the control volume nodes (e.g. P and nb). The volume associated with

[a]CDP is named after Charles David Pierce (1969–2002)

each node is computed by summing the sub-volumes of the tetrahedra, each formed by a cell center, a face, an edge and a node as shown in figure 4. This approach makes volume and surface normal calculations unambiguous and the resulting algorithm supports meshes of arbitrary convex polyhedral elements.

An overview of the unstructured finite volume method and fractional step time advancement is now given. Details of the finite volume operators and boundary condition implementation are available elsewhere.[10] A second-order fractional-step algorithm based on this non-staggered arrangement with good kinetic energy conservation properties[11,12] proceeds as follows:

1. The subgrid-scale viscosity ν_t is computed at all nodes based on the nodal velocity field u_i^n associated with the current time level t^n. The unstructured filtering operator required by the dynamic procedure consists of averaging node-based quantities to surrounding cells, then averaging the resulting cell values back to neighboring nodes. For the case of uniform hexahedral meshes, this corresponds to a top-hat spatial filter with trapezoidal rule integration.[13]

2. The edge-based normal velocity components at the new time level t^{n+1} is predicted using second-order Adams–Bashforth extrapolation:

$$\hat{U}_e = 2U_e^n - U_e^{n-1} \tag{12}$$

Note that because both U_e^n and U_e^{n-1} satisfy the discrete divergence property $\sum_e U_e A_e = 0$ (where A_e is the edge area), so will $\hat{U}_e$.

3. The following momentum equation is then solved for the node-based velocity vector u_i to get the predicted velocity $\hat{u}_i$ using the Jacobi iteration method:

$$V\frac{\hat{u}_i - u_i^n}{\Delta t} + \sum_e \overline{U_e}^t \overline{\overline{u_i}^e}^t A_e = -V\left(\frac{\delta p}{\delta x_i}\right)^{n-1/2} + \sum_e \overline{\nu+\nu_t}^e \left(\overline{\frac{\delta u_i}{\delta n}} + \overline{\frac{\delta u_n}{\delta x_i}}^e\right)^t A_e, \tag{13}$$

where V is the dual volume associated with the node (see figure 4), the averaging operator $\overline{()}^t$ corresponds to an equally weighted average in time of the known value at t_n and the predicted value at t^{n+1}, and the averaging operator $\overline{()}^e$ corresponds to the equally weighted spatial average of the two node values associated with edge e. The discrete cell-based gradient operator $\delta/\delta x_i$ is based on Green–Gauss reconstruction and the node-based normal derivative operator $\delta/\delta n$ includes non-orthogonal corrections as described in Ham *et al.*[10]

4. The old pressure gradient is subtracted from the velocity predictor and then averaged to the edges and the edge-normal component taken:

$$\frac{u_i^* - \hat{u}_i}{\Delta t} = \left(\frac{\delta p}{\delta x_i}\right)^{n-1/2} \tag{14}$$

$$U_e^* = \overline{u_i^*}^e n_i \tag{15}$$

5. The following Poisson equation for pressure is solved using an algebraic multigrid method and the starred velocity fields are corrected:

$$\sum_e \left(\frac{\delta p}{\delta n}\right)^{n+1/2} A_e = \frac{1}{\Delta t}\sum_e U_e^* A_e \tag{16}$$

$$\frac{U_e^{n+1} - U_e^*}{\Delta t} = -\left(\frac{\delta p}{\delta n}\right)^{n+1/2} \tag{17}$$

$$\frac{u_i^{n+1} - u_i^*}{\Delta t} = -\left(\frac{\delta p}{\delta x_i}\right)^{n+1/2} \tag{18}$$

A key feature of this solver is that it uses central differences for spatial discretization and constrains the numerical scheme to discretely conserve not only mass and momentum, but also kinetic energy.[14] This approach minimizes nonlinear instabilities that might arise from the complete absence of numerical dissipation at coarse-grid resolutions.

IV. Simulation overview

The flat-plate airfoil geometry is centered in the x-y plane of the computational domain of size $L_x \times L_y = 2c \times 0.5c$ and spans the length L_z of the domain in the z-direction. The aft-chord separation is induced by prescribing blowing and suction over $0.7 \leq x/c \leq 1.3$ on the top boundary of the computational domain. In all simulations of the uncontrolled separated flow presented here, the nonoperational ZNMF 'device' embedded under the airfoil upper surface is left open to the external crossflow. Comparison of the location of boundary layer separation obtained from such a simulation with one obtained without an embedded ZNMF cavity indicates that the inclusion of an inactive ZNMF device open to the external crossflow in the uncontrolled simulation does not change the separation location. The simulations of the baseline separated flow are performed on two different grids to ascertain not only the grid independency but also the spanwise domain-size independency of the computed solutions. The spanwise domain size L_z and the number of cells in the spanwise (z) direction N_z for these grids are summarized in table 1.

Table 1. Grid parameters in LES at $Re_c = 6 \times 10^4$.

Attribute	Grid I	Grid II
Overall node count	$14,486,745$	$8,920,725$
Overall cell count	$14,164,416$	$8,599,456$
L_z	$0.3c$	$0.2c$
N_z	64	32
Nodes in the wake region/N_z	$66,306$	$99,330$
Spanwise grid spacing $\Delta z/c$	4.6875×10^{-3}	6.25×10^{-3}

No-slip boundary conditions are applied on the airfoil surface, and slot and cavity walls. Slip (zero-shear) boundary condition is applied over the entire length on the lower boundary. Uniform inflow free-stream velocity is prescribed at the inlet of the computational domain. At the exit boundary, the convective outflow boundary condition is applied, with the convection speed determined by the streamwise velocity averaged across the exit plane. This outflow boundary condition allows the vortical structures from the separated region and the wake to exit the domain with minimal reflections. Consistent with the spanwise homogeneity of the flow configuration, periodic boundary conditions are prescribed on the spanwise boundaries in the z-direction. The simulations are advanced with a time step of $\Delta t U_\infty/c = 2.0 \times 10^{-4}$, which corresponds to a maximum Courant–Friedrichs–Lewy (CFL) number of around 1.6 and 2.6 on Grid I and Grid II, respectively.

First, LES of the baseline separated flow are carried out for a total time of $20c/U_\infty$, of which the first 10 time units are used to allow initial transients to exit the domain, and the time-mean flow statistics are collected over the remaining 10 time units. After confirming the grid and spanwise domain-size independency of the characteristic frequencies and mean flow properties from the LES of baseline separated flow configuration, the separated flow on the smaller grid (Grid II) at $t = 20c/U_\infty$ is advanced with ZNMF perturbation of the boundary layer at selected frequencies for a total time of $15c/U_\infty$. The first 5 time units are used to allow initial transients to exit the domain and the subsequent 10 time units are used for the computation of time-mean flow statistics.

The characteristic frequencies of the uncontrolled separated flow are determined by computing one-dimensional power spectra E_{vv} corresponding to temporal variations of crosss-stream velocity v in the shear layer, the separated region, and the wake. Flow state from Case 0 simulation at $t = 20c/U_\infty$ is then advanced with ZNMF perturbation of the boundary layer at frequencies that are harmonically related to the characteristic frequencies of the uncontrolled separated system. In the simulations with ZNMF forcing, the time step employed is the same as in the baseline simulations and the ZNMF jet velocity is set to $V_J = 0.1U_\infty$. The blowing momentum coefficient of the jet is defined as

$$c_\mu = \frac{\rho V_j^2 d}{qc} = 2\frac{d}{c}\left(\frac{V_J}{U_\infty}\right)^2 \tag{19}$$

where $q = \rho U_\infty^2/2$ is the free-stream dynamic pressure, d is the ZNMF jet slot width and c is the chord length. The choice of $V_J = 0.1U_\infty$ fixes c_μ to a value of 1.3×10^{-4}. The simulations with ZNMF forcing are

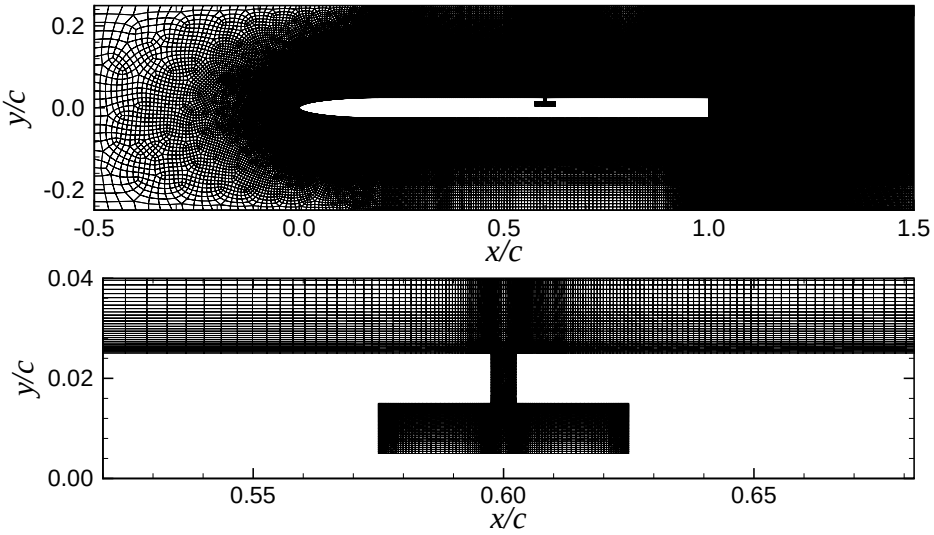

Figure 5. Computational mesh in the x–y plane of Grid II used in the large-eddy simulations.

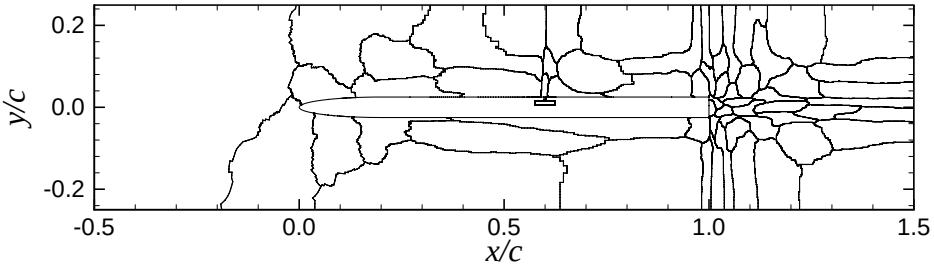

Figure 6. Domain decomposition of the mesh, shown in figure 5, obtained using ParMETIS for parallel implementation on 128 processors.

advanced for a total time of $15c/U_\infty$, of which the first 5 time units are used to allow initial transients to exit the domain and the subsequent 10 time units are used for the computation of time-mean flow statistics.

For parallel implementation, the parallel graph partitioning library ParMETIS[15] is used for domain decomposition and provides optimal load balancing with a minimal surface interface between zones. Communication between processors is achieved using Message Passing Interface (MPI) programming model. Figure 5 shows the computational mesh in the x–y plane of Grid II used in LES at $Re_c = 6 \times 10^4$, and figure 6 shows the corresponding domain decomposition obtained using ParMETIS for parallel implementation on 128 processors. Each zone in figure 6 is assigned to a separate processor for time advancement of the flow variables, and MPI is used for exchange of data at the interface between the zones during the iterative solution of the linear systems.

V. Results and Discussion

The contours of instantaneous vorticity magnitude ($|\boldsymbol{\omega}|c/U_\infty$), in the spanwise mid-plane, obtained from LES of the baseline uncontrolled separated flow (hereafter referred to as 'Case 0') at $Re_c = 6 \times 10^4$ on Grid II are presented in figure 7. As compared to its two-dimensional counterpart shown in figure 8, the LES result shows a striking difference in that the separated shear layer rolls up farther away than in 2-D simulations resulting in an open mean separation bubble as shown in the plot of mean streamlines in figure 9(a), while the 2-D direct simulations result in a closed bubble (see figure 9b). This discrepancy is in accordance with the numerical studies of flow over elliptic and circular cylinders by Mittal & Balachandar,[16] who observed that Kármán vortices roll up closer to the cylinder in 2-D simulations than in 3-D simulations resulting in increased Reynolds stresses and pressure fluctuations closer to the cylinder which in turn lead

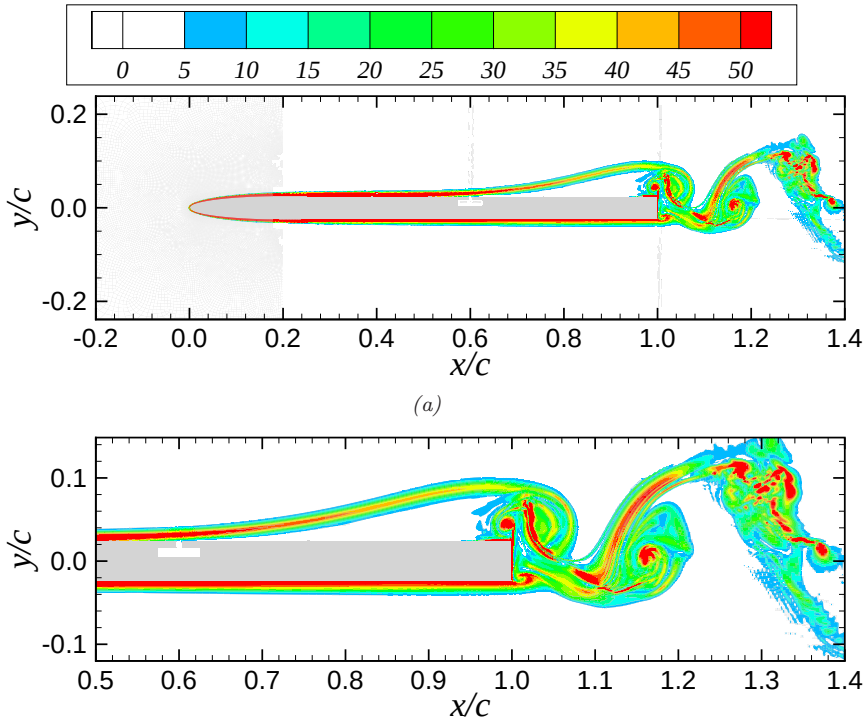

Figure 7. Contours of instantaneous vorticity magnitude ($|\boldsymbol{\omega}|c/U_\infty$) at $t = 20c/U_\infty$, in the spanwise mid-plane, obtained from LES of Case 0 at $Re_c = 6 \times 10^4$ on Grid II.

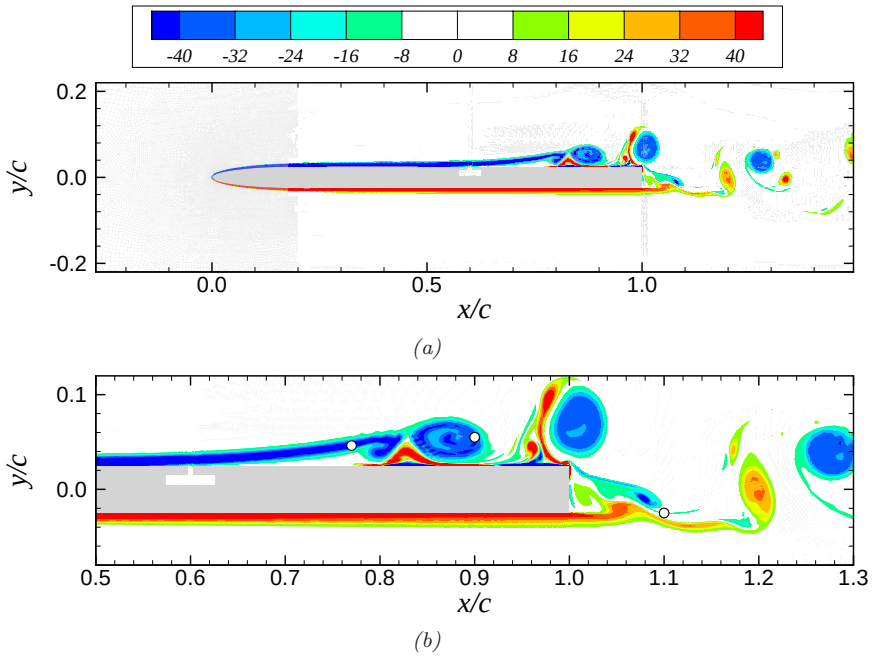

Figure 8. Contours of instantaneous spanwise vorticity ($\omega_z c/U_\infty$) at $t = 20c/U_\infty$ for the baseline separated flow at $Re_c = 6 \times 10^4$ obtained from 2-D direct simulations on Grid II by Kotapati *et al.*[3]

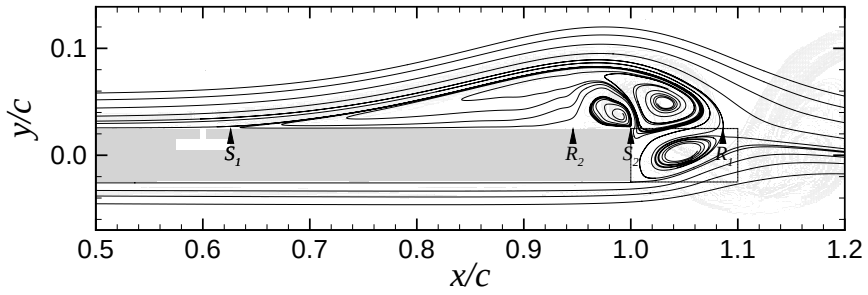

(a) LES

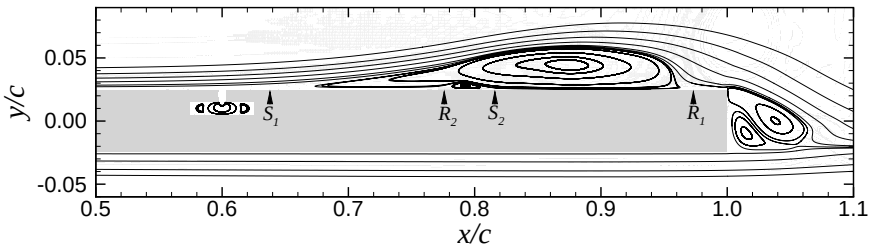

(b) 2-D direct simualtions[3]

Figure 9. Mean streamlines, in the spanwise mid-plane, obtained from LES of Case 0 at $Re_c = 6 \times 10^4$ on Grid II. Also shown are the mean streamlines obtained from 2-D direct simulations[3] on Grid II.

Table 2. Comparison of the location and size of the mean separation bubbles obtained from LES and 2-D direct simulations[3] of Case 0 at $Re_c = 6 \times 10^4$. S_1, S_2, R_1, and R_2 denote primary and secondary separation points, and primary and secondary reattachment points, respectively.

Simulation type	S_1	R_1	S_2	R_2	$L_{sep} = R_1 - S_1$	H_{sep}
LES - Grid I	$0.625c$	$1.084c$	$1.000c$	$0.947c$	$0.459c$	$0.0647c$
LES - Grid II	$0.626c$	$1.086c$	$1.000c$	$0.946c$	$0.460c$	$0.0643c$
2-D - Grid II	$0.638c$	$0.973c$	$0.811c$	$0.771c$	$0.335c$	$0.0337c$

to overprediction of the drag force in 2-D simulations. Mittal & Balachandar[16] explained this discrepancy by arguing that three-dimensional vortex stretching in 3-D simulations changes the vorticity distribution in the wake which in turn affects velocity field around the body. This results in reduced vorticity production in the attached boundary layer upstream of separation leading to the formation of weaker shear layers and the delayed roll-up in 3-D simulations.

The rolled-up vortices regularly shed from the shear layer to become one of the pair of oppositely signed vortices that constitute the Kármán vortex street in the absence of vortex shedding from the upper edge of the blunt trailing face. The vortex shedding from the upper edge of the trailing face is precluded by the presence of the secondary separation of the reverse flow induced by the vortex roll-up (see figure 9*a*). Since the open mean separation bubble obtained from LES does not have the primary reattachment point on the airfoil surface but extends beyond the trailing edge, a virtual reattachment point R_1 is defined by extending the flat plate section into the wake as shown in the plot of mean streamlines in figure 9. Table 2 compares the locations and sizes of the mean separation bubble computed using LES on Grids I and II as well as using 2-D direct simulations on Grid II. First, one finds that the data obtained on the two grids using LES are in excellent agreement with each other, thereby comfirming the independency of the simulation results with respect to the spanwise domain size, and in-plane and spanwise grid resolutions. Second, the boundary layer is found to separate earlier in the 3-D simulations than in the 2-D simulations, and the characteristic length L_{sep} and height H_{sep} of the mean separation bubble in the 3-D simulations are larger than their 2-D counterparts by 37% and 90%, respectively.

The one-dimensional power spectra E_{vv} corresponding to temporal variations of cross-stream velocity v

in the shear layer, separated region and wake, obtained from LES of Case 0 on Grids I and II are shown in figure 10. The spectrum at a given (x, y) location is obtained by averaging the power over five uniformly spaced points across the span. Also included in some of these plots are the slopes corresponding to $F^{-5/3}$ and F^{-7} variations. While the $F^{-5/3}$ variation is associated with the inertial subrange,[17] the F^{-7} variation characterizes the dissipation range[18] where most of the turbulent kinetic energy is dissipated by the action of the viscosity. Note that Taylor's hypothesis[19] is invoked, whereby the spatial correlations are approximated by temporal correlations. Figures 10(a)–(c), in that order, show the downstream development of convective instabilities in the laminar shear layer. At the streamwise location of $x/c = 0.75$, the spectra on both the grids show a peak at $fc/U_\infty = 2.14$ corresponding to the dominant frequency of the shear layer instability at this station. With the downstream development, the superharmonics at $fc/U_\infty = 4.28$ and 6.42 appear due to nonlinear interactions and grow in strength, and in particular, the superharmonic at $fc/U_\infty = 6.42$ becomes as strong as the instabililty at $fc/U_\infty = 2.14$. Also, in going from station $x/c = 0.9$ to station $x/c = 1.0$, the spectra undergo a fundamental change in the slope indicating the onset of transition of the shear layer.

The spectra in figures 10(d) and 10(e) measured downstream of the location of roll-up of shear layer show distinct peaks at $fc/U_\infty = 2.14$ corresponding to the shedding of rolled-up vortices from the shear layer as a result of an absolute instability.[20] The spectra in the wake region traversed by vortices shed from the lower edge of the trailing face, shown in figure 10(f), also indicate a strong peak at $fc/U_\infty = 2.14$. This implies that vortex shedding from the separated shear layer and from the lower edge of the trailing face, both resulting from an absolute instability,[20] lock-on and evolve together as they would in a regular Kármán vortex street in the absence of a separation bubble. Since this absolute instability is a global instability, it affects the separated shear layer upstream and modulates it at the same frequency of $fc/U_\infty = 2.14$. The other dominant superharmonic at $fc/U_\infty = 6.42$ evident in the shear layer spectra is probably close to the natural frequency of the shear layer instability and since the shear layer has a rich spectrum of response to various disturbances, it could have shifted to a superhamonic of the global wake instability. Thus,

$$f^0_{lock} = f^0_{SL} = f^0_{sep} = f^0_{wake} \approx 2.14 U_\infty/c.$$

Renormalizing the frequency $f^0_{sep}c/U_\infty$ associated with the separated region of Case 0 by the characteristic length L_{sep} of its mean separation bubble yields $f^0_{sep}L_{sep}/U_\infty \approx 1$ as in the 2-D simulations of Kotapati *et al*,[3] wherein $f^0_{lock} \approx 2.90 U_\infty/c$. This confirms that the scaling $f_{sep} \sim U_\infty/L_{sep}$ has approximately the same constant of proportionality in the 3-D simulations as in the 2-D simulations, and so the apparent decrease in $f^0_{sep}c/U_\infty$ with increase in L_{sep} in going from 2-D to 3-D simulations. Similarly, when the wake vortex shedding frequency for Case 0 is renormalized by the wake width $W_{wake} = t + H_{sep}$, one finds that $f^0_{wake}W_{wake}/U_\infty \approx 0.24$ which is the same value as that obtained in the 2-D simulations of Kotapati *et al*.

A noticeable inertial subrange and dissipation range in the spectra in figures 10(e) and 10(f) indicate completion of transition and emergence of well-developed turbulent flow at these stations. The above spectra can also be used to assess the resolutions of the two grids used in LES. The point at the higher frequencies where the spectra deviates from the F^{-7} line represents the grid cut-off, below which the frequency scales are adequately resolved, and above which they are parameterized by the SGS model. Since Grid II has twice as many points in the x–y plane than Grid I in the wake region (see table 1), the spectra in the wake show that the simulation on Grid II resolves scales much deeper into the dissipation range than the simulation on Grid I. A similar assessment can be made of the grid resolution at the other stations by looking at the corresponding spectra. Also, the overall agreement between the LES results obtained on Grids I and II with respect to the dominant frequencies and the energy levels in the range of adequately resolved frequencies further demonstrates the grid and spanwise domain size independency of the simulation results.

VI. ZNMF forcing of the separated flow

The ZNMF jet adopted in the LES produces a strictly two-dimensional mode of excitation in the absence of spanwise modulation of amplitude or phase so as to facilitate direct comparison of the LES results with their two-dimensional counterparts.[3] Further justification for adopting a two-dimensional mode of excitation over a three-dimensional mode is provided by the work of[21] that suggests that the two-dimensional mode generates the highest lift-to-drag ratio L/D at the highest C_l and produces a milder post-stall behavior than the three-dimensional mode, therefore making it a better candidate for hysteresis prevention and dynamic stall suppression in practical configurations.

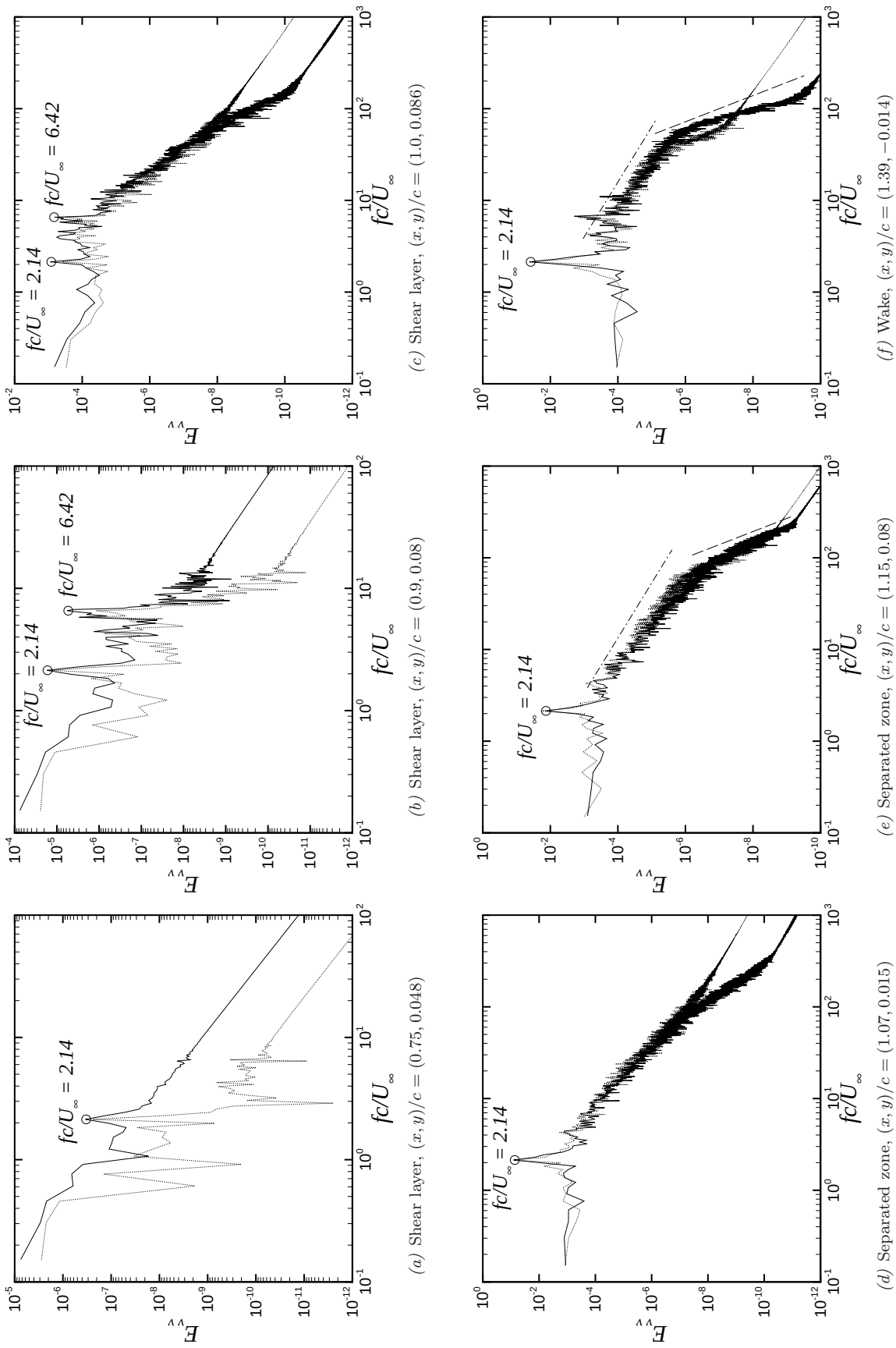

(a) Shear layer, $(x, y)/c = (0.75, 0.048)$ *(b)* Shear layer, $(x, y)/c = (0.9, 0.08)$ *(c)* Shear layer, $(x, y)/c = (1.0, 0.086)$

(d) Separated zone, $(x, y)/c = (1.07, 0.015)$ *(e)* Separated zone, $(x, y)/c = (1.15, 0.08)$ *(f)* Wake, $(x, y)/c = (1.39, -0.014)$

Figure 10. Spanwise-averaged power spectra corresponding to the temporal variations of cross-stream velocity, in the shear layer (*a–c*), separation zone (*d–e*) and wake (*f*), obtained from LES of Case 0 at $Re_c = 6 \times 10^4$ on Grids I and II. ·····, Grid I; ———, Grid II; —·—, $F^{-5/3}$; – – –, F^{-7}.

Table 3. Various LES cases resulting from ZNMF forcing of the baseline separated flow obtained from LES at $Re_c = 6 \times 10^4$ and $V_J/U_\infty = 0.1$.

Case	$f_J/f^0_{lock-on}$	$F^+_J = f_J c/U_\infty$
1	1	2.14
2	2	4.28
3	3	6.42
4	4	8.56
5	10	21.40

Because of the enormous computational cost associated with these 3-D simulations, in what follows, the effect of ZNMF forcing on the separated flow in the 3-D simulations is studied using only Grid II which has higher resolution in the wake and yet a smaller overall grid size owing to smaller spanwise extent and lower spanwise resolution as compared to Grid I. Based on the control effectiveness observed in the 2-D simulations,[3] the separated flow obtained by LES of Case 0 is subjected to ZNMF forcing at only five representative frequencies as shown in table 3.

Figures 11(a)–(e) show the contours of instantaneous vorticity magnitude ($|\boldsymbol{\omega}|c/U_\infty$), in the spanwise mid-plane, obtained from LES of Cases 1–5, respectively, on Grid II. As compared to Case 0, ZNMF forcing in Cases 1–4 is clearly seen to advance the discretization and/or roll-up of the separated shear layer, besides reducing the height of the separated region significantly. Comparing ZNMF forcing in Cases 1–4 at $f_J/f^0_{lock-on} = 1$, 2, 3 and 4 in the 3-D simulations with their 2-D counterparts[3] (see figures 12), one finds that even though 3-D solution shows a wide range of spatial scales owing to three-dimensional vortex stretching, the large scale features are very similar in both 2-D and 3-D simulations, therefore implying two-dimensionalization of the gross flow due to ZNMF forcing.

The shear layer is also seen to undergo earlier transition to turbulence in Cases 1–4 than in Case 0. However, this accelerated laminar–turbulent transition does not play as significant a role in separation control as the large coherent structures that result from the discretization of the shear layer due to ZNMF forcing. For instance, the separated region beyond $x/c = 0.85$ in Case 4 is turbulent (as will also be shown later using power spectra), yet the corresponding plot of mean streamlines in figure 13(d) shows a large mean separation bubble similar to that observed with forcing at $f_J = 4f^0_{lock}$ in 2-D simulations. On the other hand, even though the separated shear layer in Cases 1 and 2 is laminar or only transitioning to turbulence, the large coherent structures generated by ZNMF forcing entrain high-momemtum fluid from the outer flow into the near-wall region, thereby reducing the size of the mean separation bubble dramatically as shown in figures 13(a) and 13(b) for Cases 1 and 2, respectively. In particular, of the five cases considered, the forcing at $f_J = 2f_{lock}$ in Case 2 generates a train of vortices close to the wall that leads to regularization of the flow field and most effective separation control. On the other hand, high-frequency forcing in Case 5 has no effect on the separated shear layer, resulting in same flow dynamics as Case 0.

Although the purpose of these large-eddy simulations is to study the effect of three-dimensionality on the scaling of the characterictic frequencies of the separated flow and its subsequent control, it is nevertheless insightful to assess the role played by the dynamic SGS model in the simulations. Figures 14(a)–(f) show contour plots of mean normalized SGS eddy viscosity $\langle \nu_T/\nu \rangle$, in the spanwise mid-plane, for Cases 0–5, respectively. The corresponding contour plots of the turbulent kinetic energy $\langle u_i u_i \rangle/(2U^2_\infty)$ are shown in figures 15(a)–(f), respectively. First, the highest values of the SGS eddy viscosity for Case 0 occur in the wake where, as will be shown using power spectra in the following pages, the separated shear layer and the vortices shed from the pressure side undergo transition to turbulence. These locations where SGS eddy viscosity peaks also correspond to where the turbulent kinetic energy shown in figure 15(a) reaches its maximum. Thus, the dynamic SGS model, whose primary function is to mimic the drain of turbulent kinetic energy associated with the energy cascade, introduces dissipation in regions of significant turbulent fluctuations to remove the energy from the resolved scales and limits SGS eddy viscosity to near-zero values in regions where the flow is unsteady but not turbulent.

Next, because the ZNMF forcing in Cases 1, 3 and 4 leads to earlier transition to turbulence in the separated region and particularly higher strain rate in Case 4 due to subharmonic pairing of vortices, highest

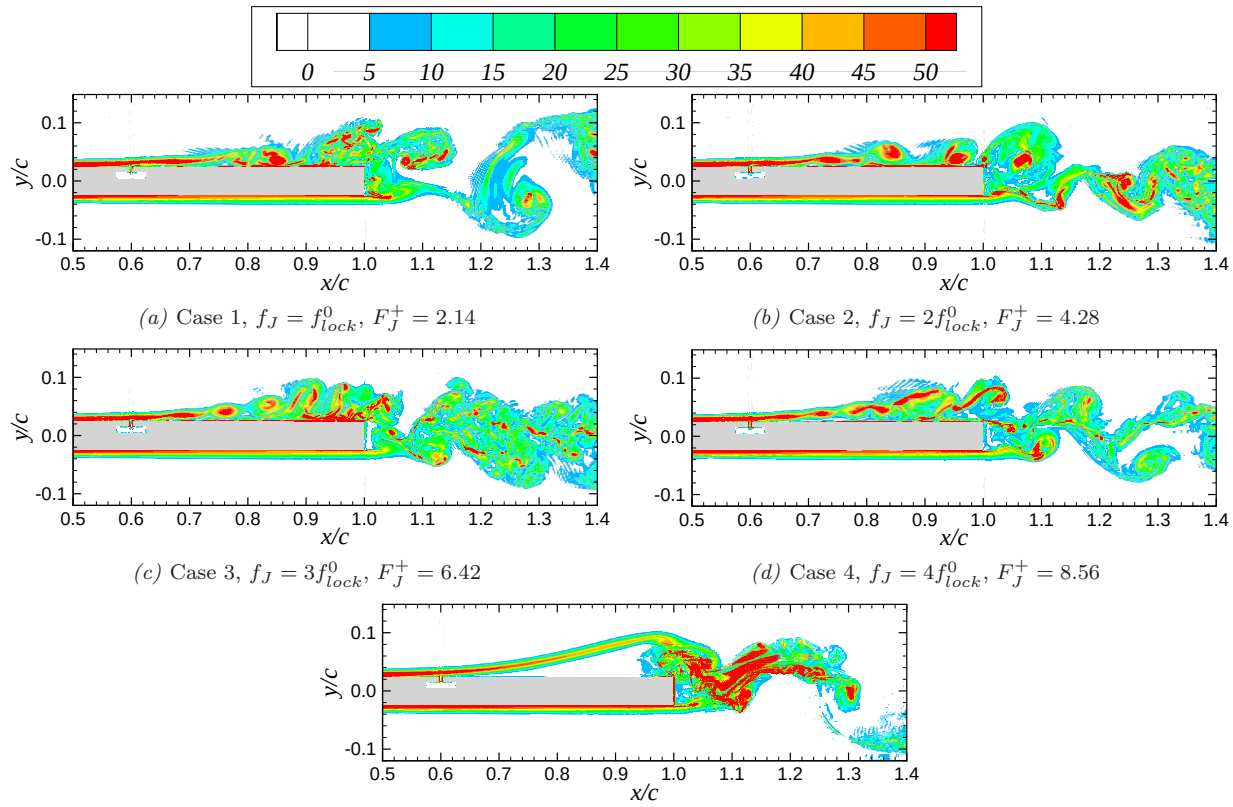

(a) Case 1, $f_J = f^0_{lock}$, $F^+_J = 2.14$

(b) Case 2, $f_J = 2f^0_{lock}$, $F^+_J = 4.28$

(c) Case 3, $f_J = 3f^0_{lock}$, $F^+_J = 6.42$

(d) Case 4, $f_J = 4f^0_{lock}$, $F^+_J = 8.56$

(e) Case 5, $f_J = 10f^0_{lock}$, $F^+_J = 21.4$

Figure 11. Contours of instantaneous vorticity magnitude ($|\boldsymbol{\omega}|c/U_\infty$) at $t = 35c/U_\infty$, in the spanwise mid-plane, obtained from LES of Cases 1–5 on Grid II.

values of SGS eddy viscosity are seen in the separated region. However, for Case 2, since ZNMF forcing results in regularization of the flow field leading to maximal flow attachment, the eddy viscosity levels in the separated region are considerably lower than those for other cases. Also, the two distinct strands seen in the contour plot of $\langle \nu_T/\nu \rangle$ in the wake region for cases 0 and 5 indicate a well-organized Kármán vortex street. The apparent reduction in the intensity of turbulent kinetic energy for Cases 1–4 shown in figures 15(b)–(e), respectively, is caused by ZNMF forcing that suppresses random unsteadiness and increases coherence of the flow structures.

The mean pressure $\langle C_p \rangle$ distribution on the spanwise mid-section of the airfoil obtained from LES of Cases 0–5 is plotted in figure 16. Also plotted in this figure is the distribution for Case 0 computed on Grid I. First, the distributions for Case 0 computed on Grids I and II show reasonable agreement, confirming the independency of the surface pressure with respect to spanwise domain size, and in-plane and spanwise grid resolutions. Second, as compared to $\langle C_p \rangle$ from the 2-D simulations shown in the figure 17, $\langle C_p \rangle$ distribution computed using LES shows much lower suction peak. As explained by,[16] this lower suction peak in 3-D simulations is attributed to the establishment of three-dimensionality in the wake that changes the wake vorticity distribution, which in turn affects the entire velocity field and reduces the vorticity distribution and production on the surface. Since the tangential pressure gradient, and therefore the mean pressure distribution, is determined by the vorticity source strength on the surface, reduced vorticity production in the 3-D simulations leads to reduced pressure distribution. As discussed earlier, this reduced vorticity production also leads to delayed roll-up of the separated shear layer, which in turn, closes this cycle of processes. $\langle C_p \rangle$ for Case 0 from LES also shows a large pressure plateau corresponding to the separated region.

The pressure distributions for Cases 1 and 2 with ZNMF forcing at $f_J = f^0_{lock}$ and $2f^0_{lock}$, respectively, look very similar to their 2-D counterparts in figure 17, implying that the ZNMF forcing in the 3-D simulations drives the bulk flow toward its two-dimensional state. Although forcing at $f_J = 4f^0_{lock}$ in Case 4 closes the

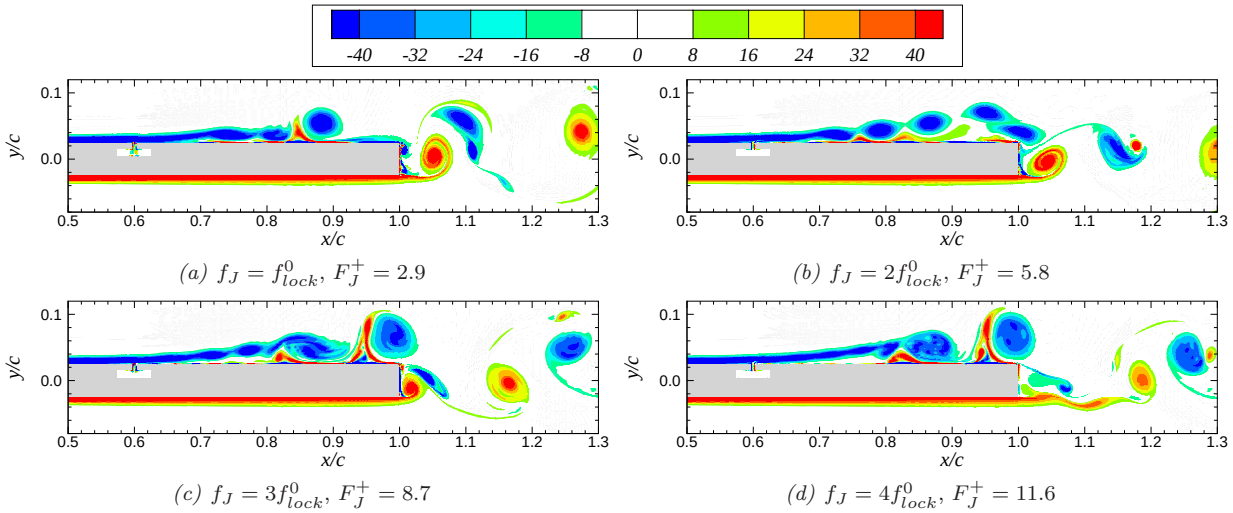

(a) $f_J = f^0_{lock}$, $F^+_J = 2.9$ (b) $f_J = 2f^0_{lock}$, $F^+_J = 5.8$

(c) $f_J = 3f^0_{lock}$, $F^+_J = 8.7$ (d) $f_J = 4f^0_{lock}$, $F^+_J = 11.6$

Figure 12. Contours of instantaneous spanwise vorticity ($\omega_z c/U_\infty$) at $t = 35c/U_\infty$ from direct simulations of Cases 1–4 on Grid II.

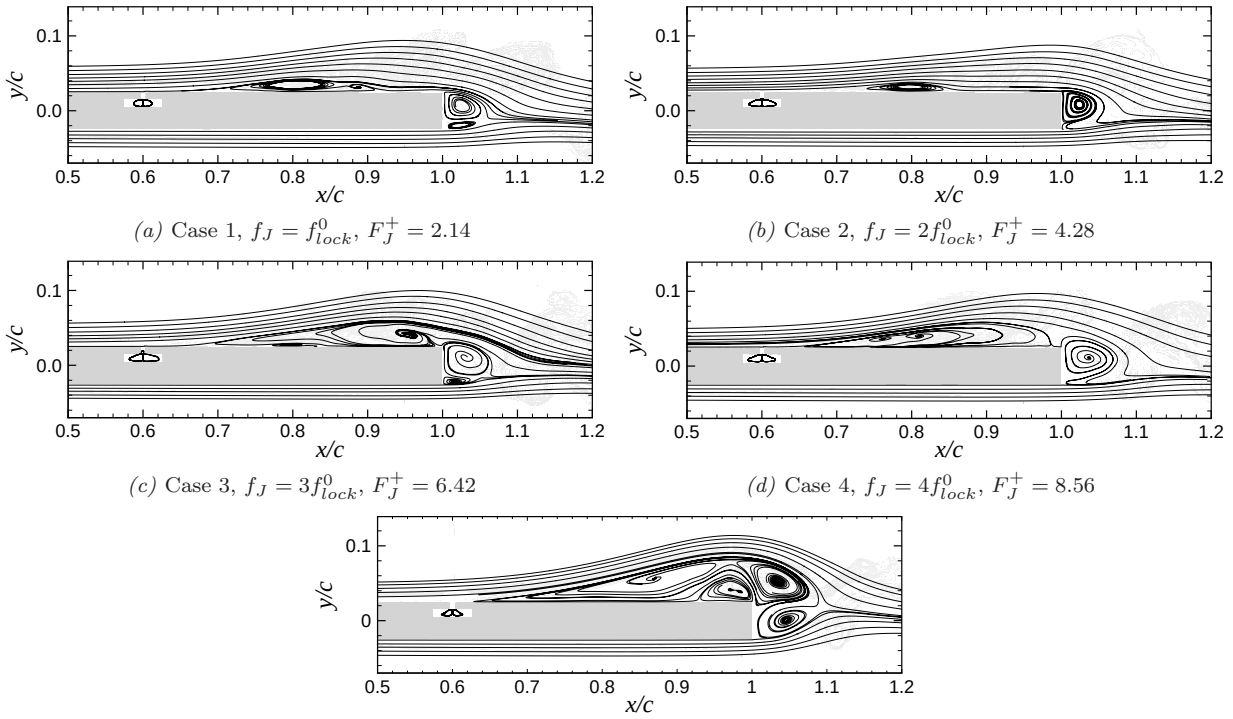

(a) Case 1, $f_J = f^0_{lock}$, $F^+_J = 2.14$ (b) Case 2, $f_J = 2f^0_{lock}$, $F^+_J = 4.28$

(c) Case 3, $f_J = 3f^0_{lock}$, $F^+_J = 6.42$ (d) Case 4, $f_J = 4f^0_{lock}$, $F^+_J = 8.56$

(e) Case 5, $f_J = 10f^0_{lock}$, $F^+_J = 21.4$

Figure 13. Mean streamlines, in the spanwise mid-plane, obtained from LES of Cases 1–3 at $Re_c = 6 \times 10^4$ on Grid II.

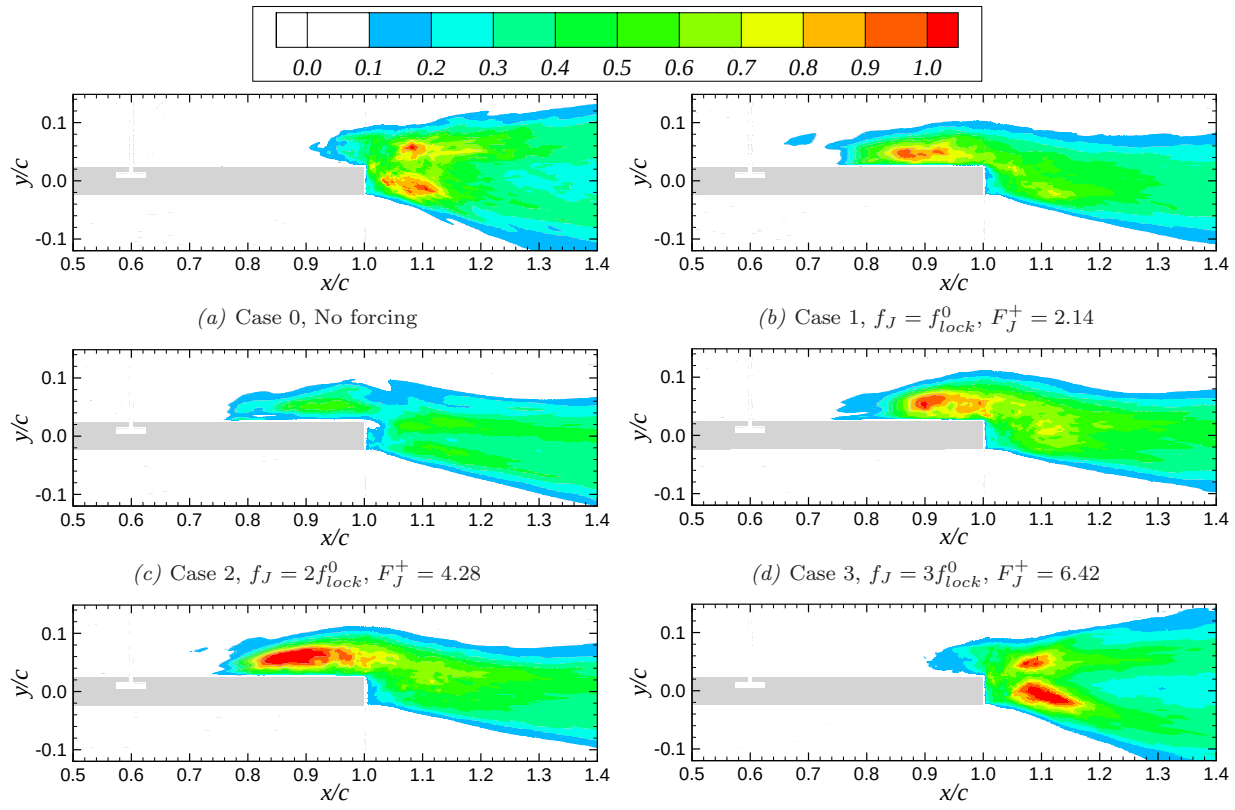

(a) Case 0, No forcing

(b) Case 1, $f_J = f^0_{lock}$, $F^+_J = 2.14$

(c) Case 2, $f_J = 2f^0_{lock}$, $F^+_J = 4.28$

(d) Case 3, $f_J = 3f^0_{lock}$, $F^+_J = 6.42$

(e) Case 4, $f_J = 4f^0_{lock}$, $F^+_J = 8.56$

(f) Case 5, $f_J = 10f^0_{lock}$, $F^+_J = 21.4$

Figure 14. Contours of mean SGS eddy viscosity $\langle \nu_T/\nu \rangle$, in the spanwise mid-plane, obtained from LES of Cases 0–5 on Grid II.

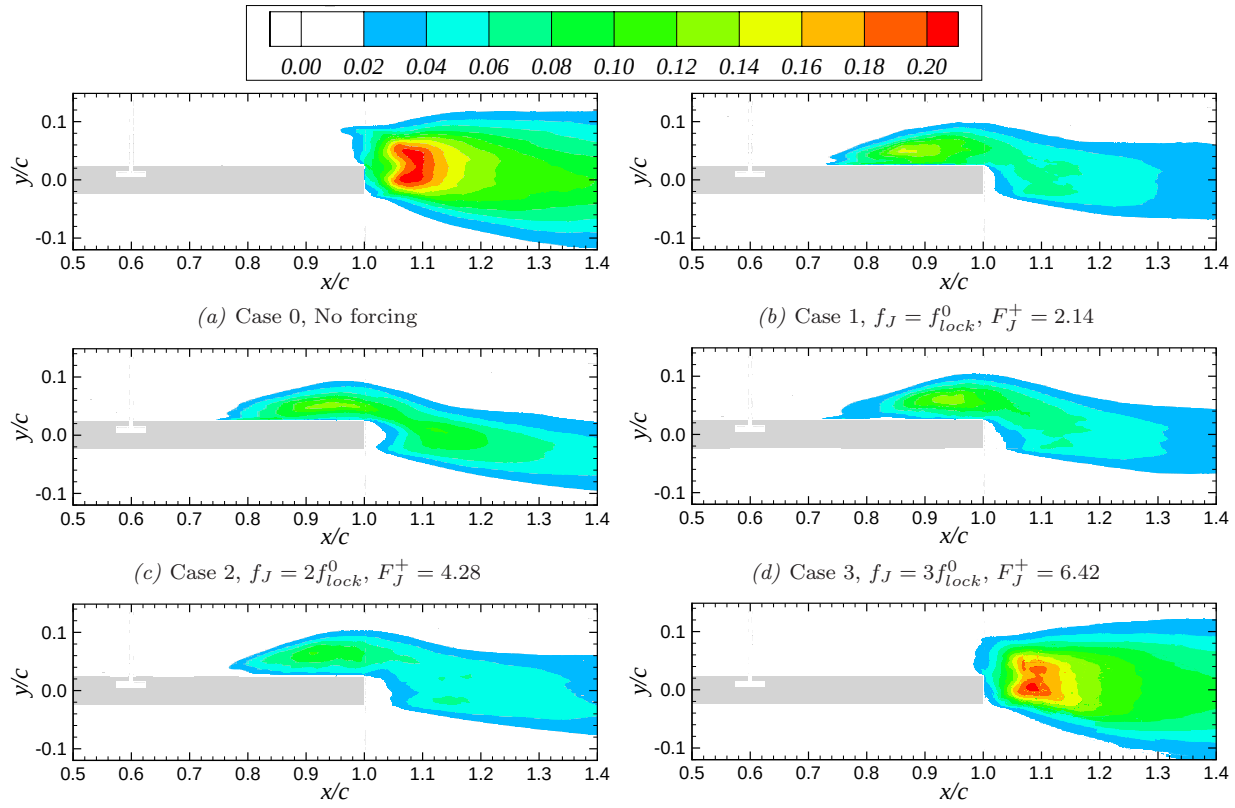

(a) Case 0, No forcing

(b) Case 1, $f_J = f^0_{lock}$, $F^+_J = 2.14$

(c) Case 2, $f_J = 2f^0_{lock}$, $F^+_J = 4.28$

(d) Case 3, $f_J = 3f^0_{lock}$, $F^+_J = 6.42$

(e) Case 4, $f_J = 4f^0_{lock}$, $F^+_J = 8.56$

(f) Case 5, $f_J = 10f^0_{lock}$, $F^+_J = 21.4$

Figure 15. Contours of mean turbulent kinetic energy $\langle u_i u_i \rangle / (2U^2_\infty)$, in the spanwise mid-plane, obtained from LES of Cases 0–5 on Grid II.

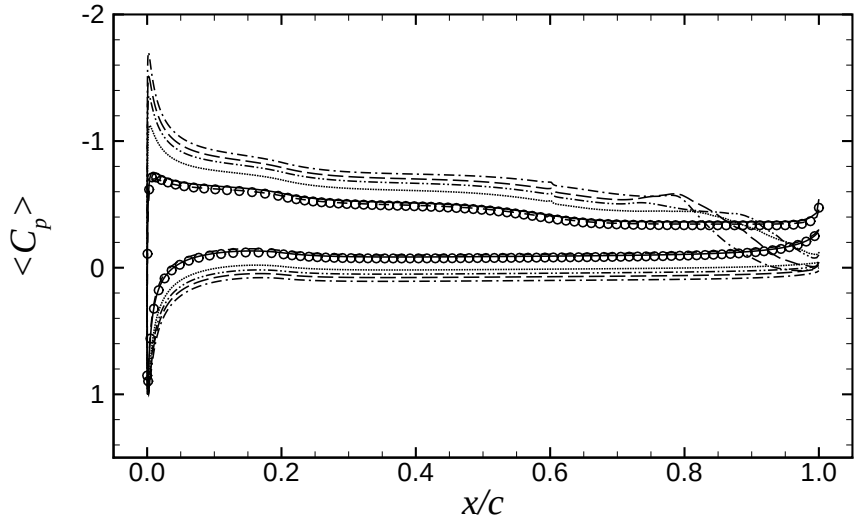

(a)

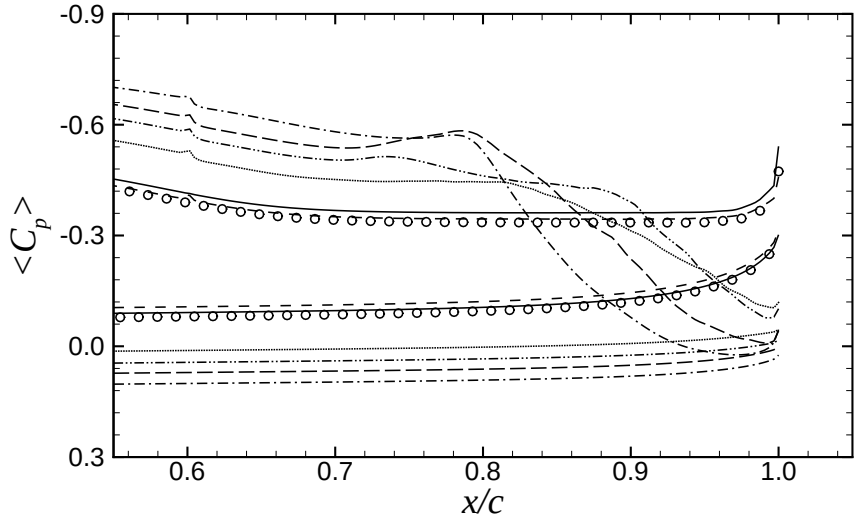

(b)

Figure 16. Mean pressure coefficient $\langle C_p \rangle$, on the spanwise mid-section of the airfoil surface, obtained from LES of Cases 0–3 at $Re_c = 6 \times 10^4$. Grid I: ∘ , Case 0. Grid II: ——— , Case 0 (No forcing); – – – , Case 1 ($f_J = f^0_{lock}$); —·— , Case 2 ($f_J = 2f^0_{lock}$); —··— , Case 3 ($f_J = 3f^0_{lock}$); ····· , Case 4 ($f_J = 4f^0_{lock}$); – – – – , Case 5 ($f_J = 10f^0_{lock}$).

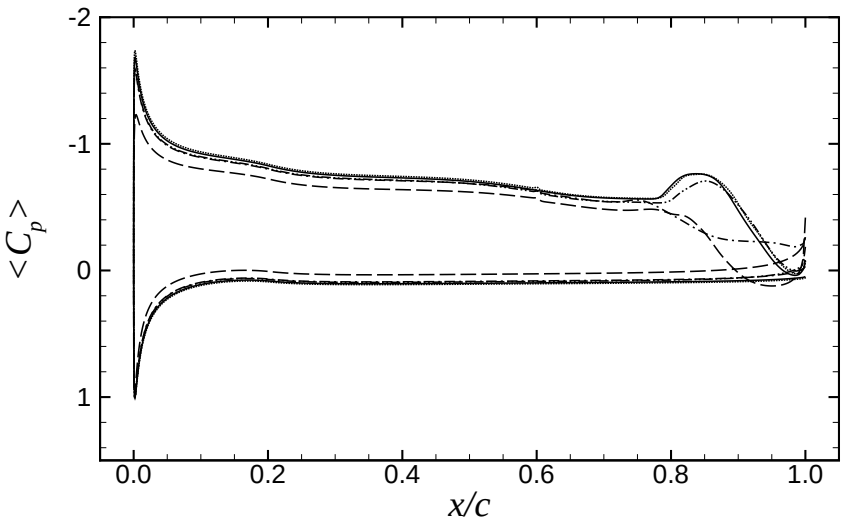

Figure 17. Pressure distribution C_p on the airfoil surface obtained from direct simulations of Cases 0–4 on Grid II by Kotapati *et al.*[3] ——— , Case 0 (No forcing); – – – , Case 1 ($f_J = f^0_{lock}$); —·— , Case 2 ($f_J = 2f^0_{lock}$); —··— , Case 3 ($f_J = 3f^0_{lock}$); ····· , Case 4 ($f_J = 4f^0_{lock}$).

mean separation bubble upstream of the trailing edge, lack of effectiveness of further control results in only a marginal pressure recovery in the aft-section. On the other hand, dramatic reduction in the size of the mean separation bubble due to forcing at $f_J = f^0_{lock}$ and $2f^0_{lock}$ in Cases 1 and 2, respectively, results in increased pressure distribution on the entire airfoil owing to increased circulation around the airfoil, and in particular, higher rates of pressure recovery in the aft-section. Using the rate of pressure recovery as a measure of separation control, one finds forcing at $f_J = 2f^0_{lock}$ to be the most effective of the five cases considered.

Figure 18 shows the distributions of streamwise local mean skin-friction coefficient $\langle C_f \rangle$, in the aft-chord region of the spanwise mid-section of the airfoil, obtained from LES of Cases 0–5 on Grid II. Distribution of $\langle C_f \rangle$ for Case 0 computed on Grid I is also included and shows excellent agreement with the data obtained on Grid II. A drop in the value of $\langle C_f \rangle$ for all cases at $x/c = 0.6$ indicates the presence of ZNMF slot at that location. It should be pointed out that the change in the sign of $\langle C_f \rangle$ for Case 0 at $x/c \approx 0.94$ does not correspond to primary reattachment point R_1, but to secondary reattachment point R_2 of the separated flow induced by the roll-up of the shear layer immediately downstream of the trailing edge (see figures 7*b* and 9*a*). Therefore, the streamwise extent $0.63 \leq x/c \leq 0.94$ in Case 0 corresponds to the so-called 'dead air' region, where the reversed flow has very low streamwise velocity, thereby resulting in low negative values of $\langle C_f \rangle$. However, high-speed secondary recirculation induced by vortex roll-up results in large positive values of $\langle C_f \rangle$ near the trailing edge. On the other hand, $\langle C_f \rangle = 0$ at the most downstream location in Cases 1–4 does correspond to the primary reattachment point R_1 owing to the closing of the mean separation bubble upstream of the trailing edge with ZNMF forcing.

With ZNMF forcing in Cases 1 and 2, the separation bubble reduces in size from both the sides, i.e. not only does the primary reattachment point R_1 move upstream, but also the primary separation point S_1 moves downstream.[22] attributed such a two-sided reduction in the size of the mean separation bubble to a feedback effect resulting from mean flow deformation caused by ZNMF forcing. Larger negative values of $\langle C_f \rangle$ in the separated region for Cases 1–4 than those for Cases 0 and 5 arise from the downstream convection of large coherent vortices formed from the discretization of the separated shear layer. $\langle C_f \rangle$ distribution for Case 1 also shows secondary separation and reattachment of the induced flow caused by vortex roll-up. Based on the criterion of maximal flow attachment as defined by wall shear stress, amongst the five cases with ZNMF forcing, Case 2 with forcing at $f_J = 2f^0_{lock}$ results in most effective separation control. Table 4 summarizes the location and size of the mean separation bubbles obtained from LES of Cases 1–5 on Grid II.

The spanwise-averaged power spectra corresponding to temporal variations of cross-stream velocity v in the shear layer, separated region and wake, obtained from LES of Cases 1–5 on Grid II are shown in figures 19–23, respectively. The slopes corresponding to $F^{-5/3}$ and F^{-7} variations corresponding to the inertial subrange and dissipation range, respectively, as discussed before, are also included in some of these

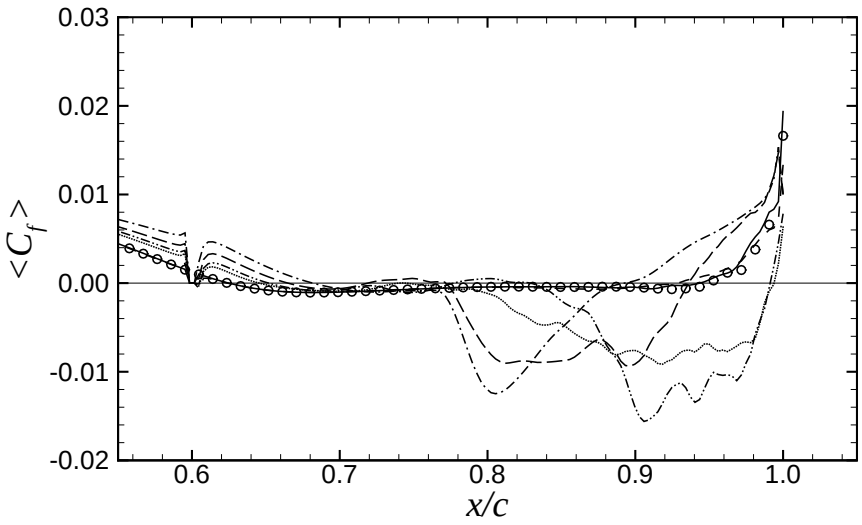

Figure 18. Distribution of streamwise local mean skin-friction coefficient $\langle C_f \rangle$, on the spanwise mid-section of the airfoil surface, obtained from LES of Cases 0–3 at $Re_c = 6 \times 10^4$. Grid I: ∘ , Case 0. Grid II: ——— , Case 0 (No forcing); – – – , Case 1 ($f_J = f^0_{lock}$); —·— , Case 2 ($f_J = 2f^0_{lock}$); —··— , Case 3 ($f_J = 3f^0_{lock}$); ····· , Case 4 ($f_J = 4f^0_{lock}$); - - - - , Case 5 ($f_J = 10f^0_{lock}$).

Table 4. Location and size of the mean separation bubble obtained from LES of Cases 1–3 at $Re_c = 6 \times 10^4$ on Grid II.

Case	S_1	R_1	$L_{sep} = R_1 - S_1$	H_{sep}
1	$0.6659c$	$0.9342c$	$0.2683c$	$0.0170c$
2	$0.6828c$	$0.8959c$	$0.2131c$	$0.0118c$
3	$0.6617c$	$0.9907c$	$0.3290c$	$0.0349c$
4	$0.6466c$	$0.9926c$	$0.3460c$	$0.0336c$
5	$0.6242c$	$1.0897c$	$0.4655c$	$0.0601c$

plots. For cases with forcing that results in effective control (i.e. cases 1–4), the forcing frequency shows up as the most dominant frequency in the spectra of shear layer at the location of ZNMF jet actuation. However, nonlinear interaction of the ZNMF jet with the shear layer instabilities also gives rise to superharmonics that grow in amplitude with downstream development. Whereas the superharmonics become dominant over the forcing frequency and govern the roll-up of the shear layer in Case 1 (see figures 19*a*–19*c*), the forcing frequency remains the dominant frequency over the entire length of the separated shear layer in Cases 2, 3 and 4 (figures 20*a*–20*c*, 21*a*–21*c* and 22*a*–22*c*). This is in accordance with the spectral dynamics of the shear layer observed in the 2-D simulations. The ZNMF forcing is also seen to suppress random high-frequency modes and sustain only the forcing frequency and its superharmonics in the shear layer. Sustained amplification of the Kelvin–Helmholtz instability in Case 4 due to ZNMF forcing transitions the laminar shear layer to turbulence as is evident in the spectrum in figure 22(*c*) that shows distinct inertial subrange and dissipation range corresponding to turbulent flow.

While in Case 1, only the pinch-off of the rolled-up vortices from the shear layer and the wake vortex shedding from the pressure side are locked on to the forcing frequency, the ZNMF forcing at $f_J = 2f^0_{lock}$ in Case 2 causes the entire system to lock on to the fundamental forcing frequency. Also, only in Case 2 does ZNMF forcing suppress random high-frequency modes in the entire flow field suggesting strongest resonance at $f_J = 2f^0_{lock}$ which then translates to most effective separation control as observed previously. On the other hand, because the separated shear layer transitions to turbulence in Case 4, the rolled-up vortices are less coherent and therefore fail to register a distinct peak in the spectrum shown in figure 21(*d*). For all cases, a well-developed turbulent flow is found to be established in the wake at least within 40% of the chord

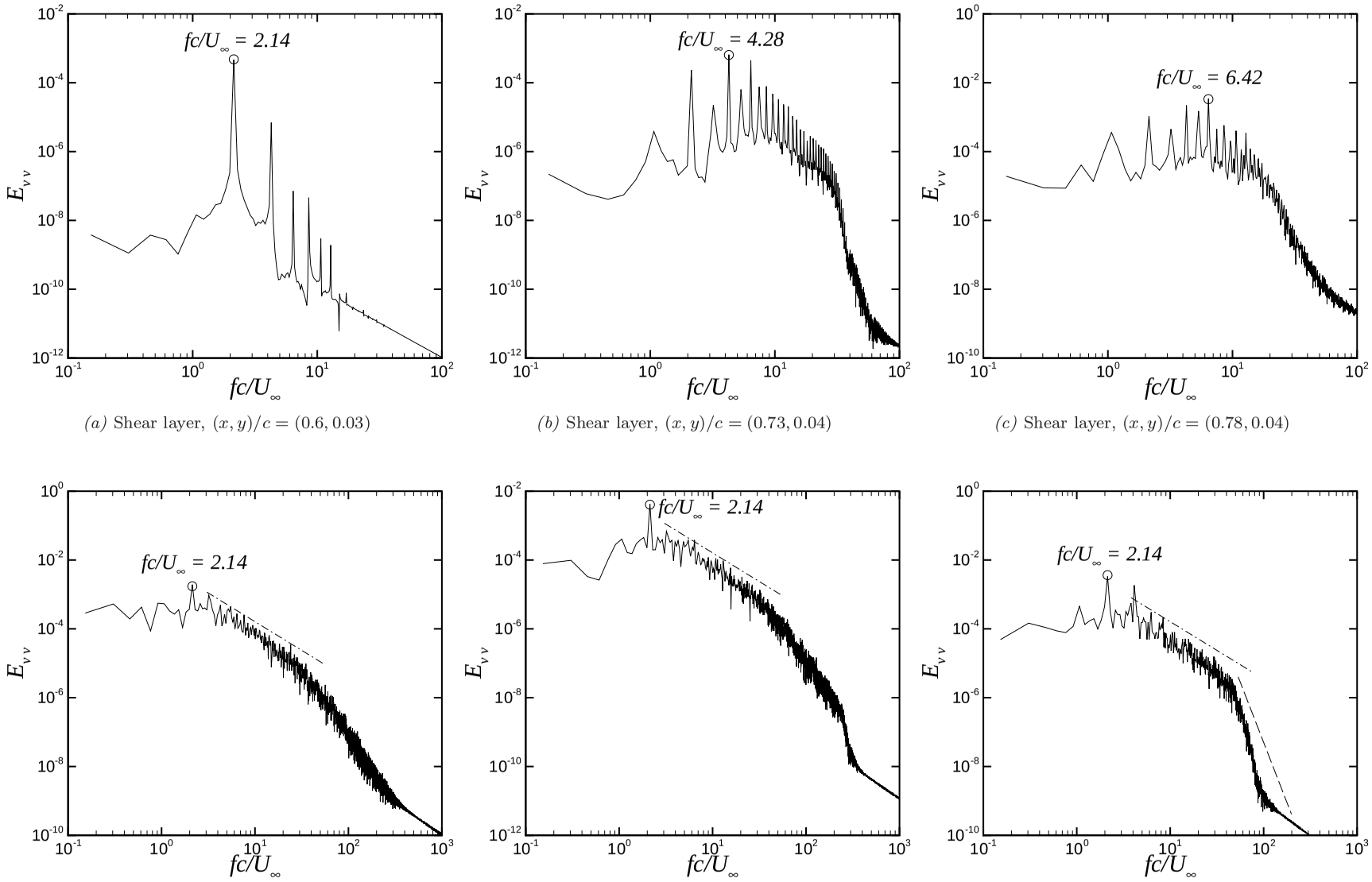

(a) Shear layer, $(x, y)/c = (0.6, 0.03)$

(b) Shear layer, $(x, y)/c = (0.73, 0.04)$

(c) Shear layer, $(x, y)/c = (0.78, 0.04)$

(d) Separated zone, $(x, y)/c = (1.00, 0.05)$

(e) Separated zone, $(x, y)/c = (1.05, 0.065)$

(f) Wake, $(x, y)/c = (1.39, -0.014)$

Figure 19. Spanwise-averaged power spectra corresponding to the temporal variations of cross-stream velocity, in the shear layer (*a*–*c*), separation zone (*d*–*e*) and wake (*f*), obtained from LES of Case 1 ($f_J = f^0_{lock}$) on Grid II. ——— , E_{vv}; —·— , $F^{-5/3}$; – – – , F^{-7}.

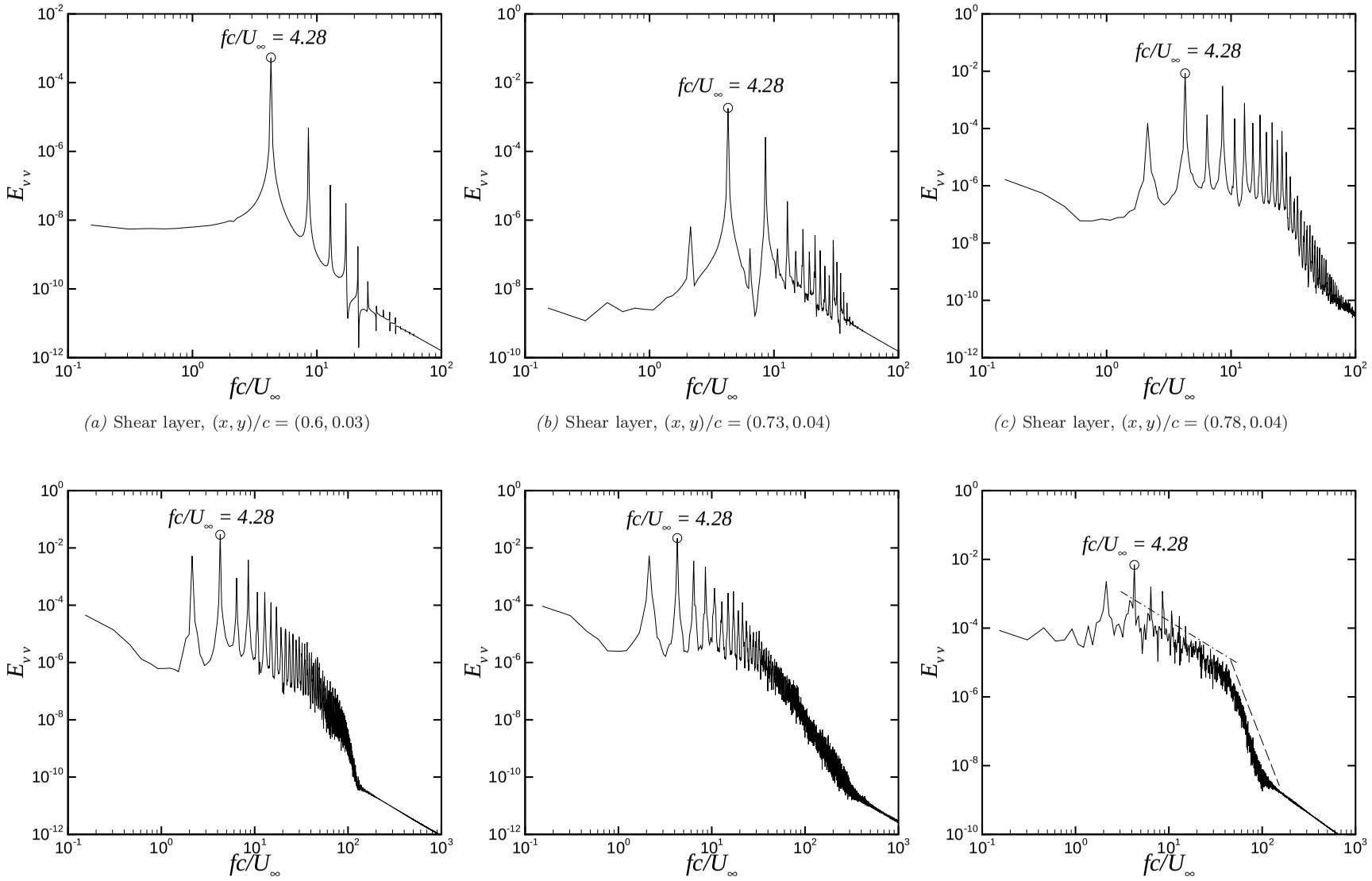

(a) Shear layer, $(x, y)/c = (0.6, 0.03)$

(b) Shear layer, $(x, y)/c = (0.73, 0.04)$

(c) Shear layer, $(x, y)/c = (0.78, 0.04)$

(d) Separated zone, $(x, y)/c = (0.9, 0.06)$

(e) Separated zone, $(x, y)/c = (1.0, 0.05)$

(f) Wake, $(x, y)/c = (1.39, -0.014)$

Figure 20. Spanwise-averaged power spectra corresponding to the temporal variations of cross-stream velocity, in the shear layer (*a*–*c*), separation zone (*d*–*e*) and wake (*f*), obtained from LES of Case 2 ($f_J = 2f^0_{lock}$) on Grid II. ——— , E_{vv}; —·— , $F^{-5/3}$; – – – , F^{-7}.

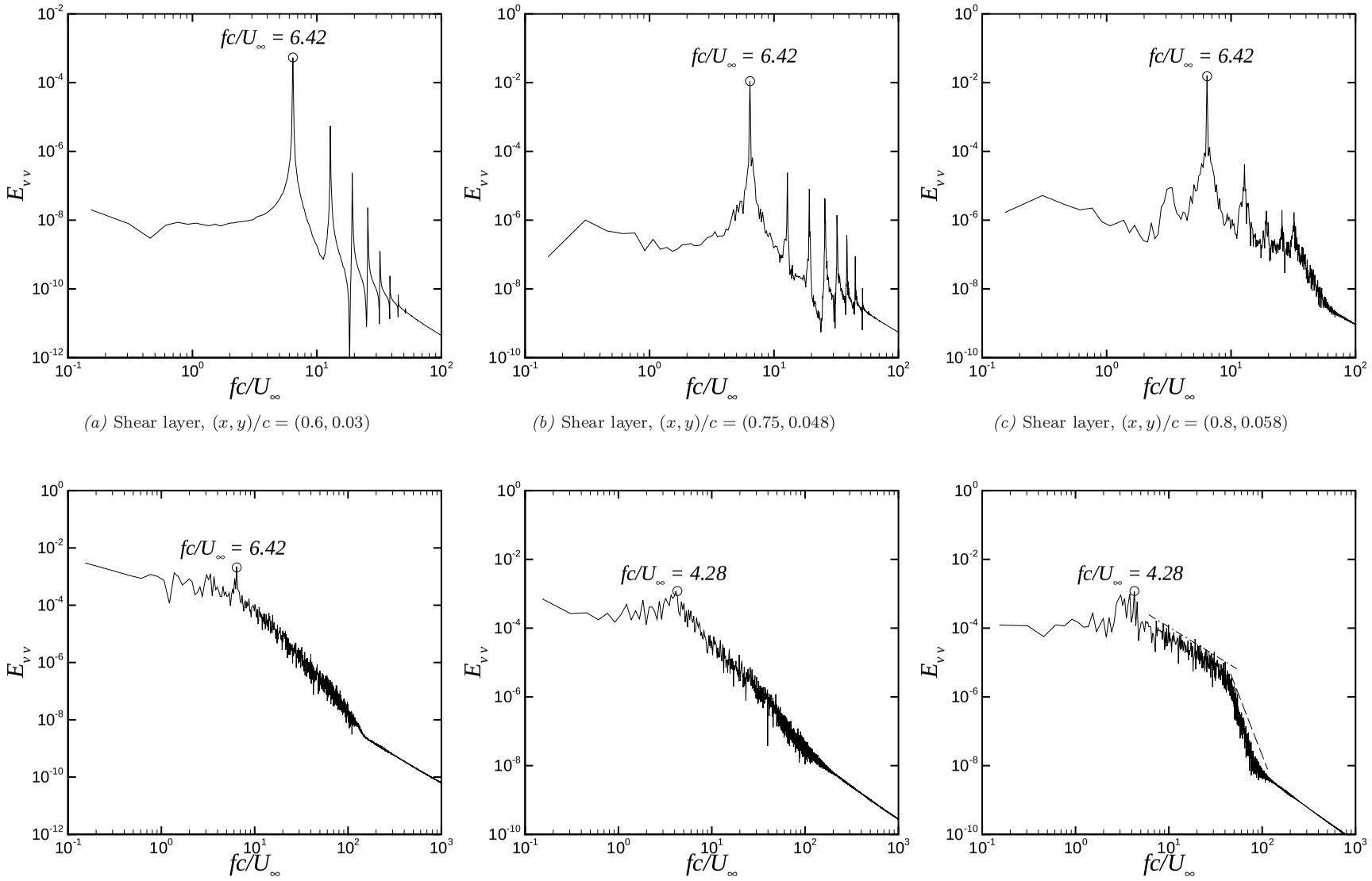

(a) Shear layer, $(x, y)/c = (0.6, 0.03)$ *(b)* Shear layer, $(x, y)/c = (0.75, 0.048)$ *(c)* Shear layer, $(x, y)/c = (0.8, 0.058)$

(d) Separated zone, $(x, y)/c = (0.95, 0.05)$ *(e)* Wake, $(x, y)/c = (1.09, -0.02)$ *(f)* Wake, $(x, y)/c = (1.39, -0.014)$

Figure 21. Spanwise-averaged power spectra corresponding to the temporal variations of cross-stream velocity, in the shear layer (*a*–*c*), separation zone (*d*) and wake (*e*–*f*), obtained from LES of Case 3 ($f_J = 3f^0_{lock}$) on Grid II. ——— , E_{vv}; —·— , $F^{-5/3}$; – – – , F^{-7}.

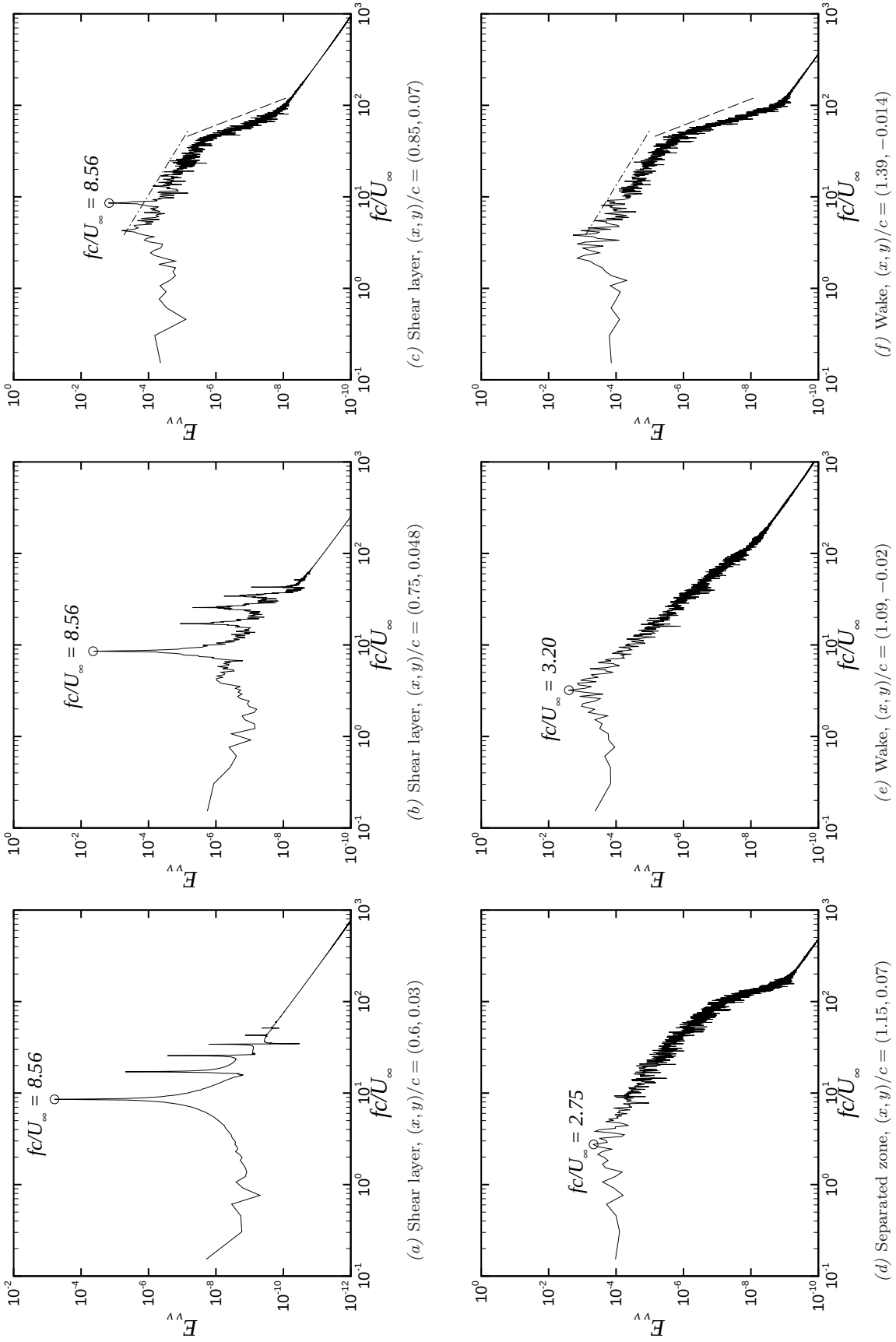

(a) Shear layer, $(x, y)/c = (0.6, 0.03)$ *(b)* Shear layer, $(x, y)/c = (0.75, 0.048)$ *(c)* Shear layer, $(x, y)/c = (0.85, 0.07)$

(d) Separated zone, $(x, y)/c = (1.15, 0.07)$ *(e)* Wake, $(x, y)/c = (1.09, -0.02)$ *(f)* Wake, $(x, y)/c = (1.39, -0.014)$

Figure 22. Spanwise-averaged power spectra corresponding to the temporal variations of cross-stream velocity, in the shear layer (*a*–*c*), separation zone (*d*) and wake (*e*–*f*), obtained from LES of Case 4 ($f_J = 4 f^0_{lock}$) on Grid II. ——— , E_{vv}; —·— , $F^{-5/3}$; – – – , F^{-7}.

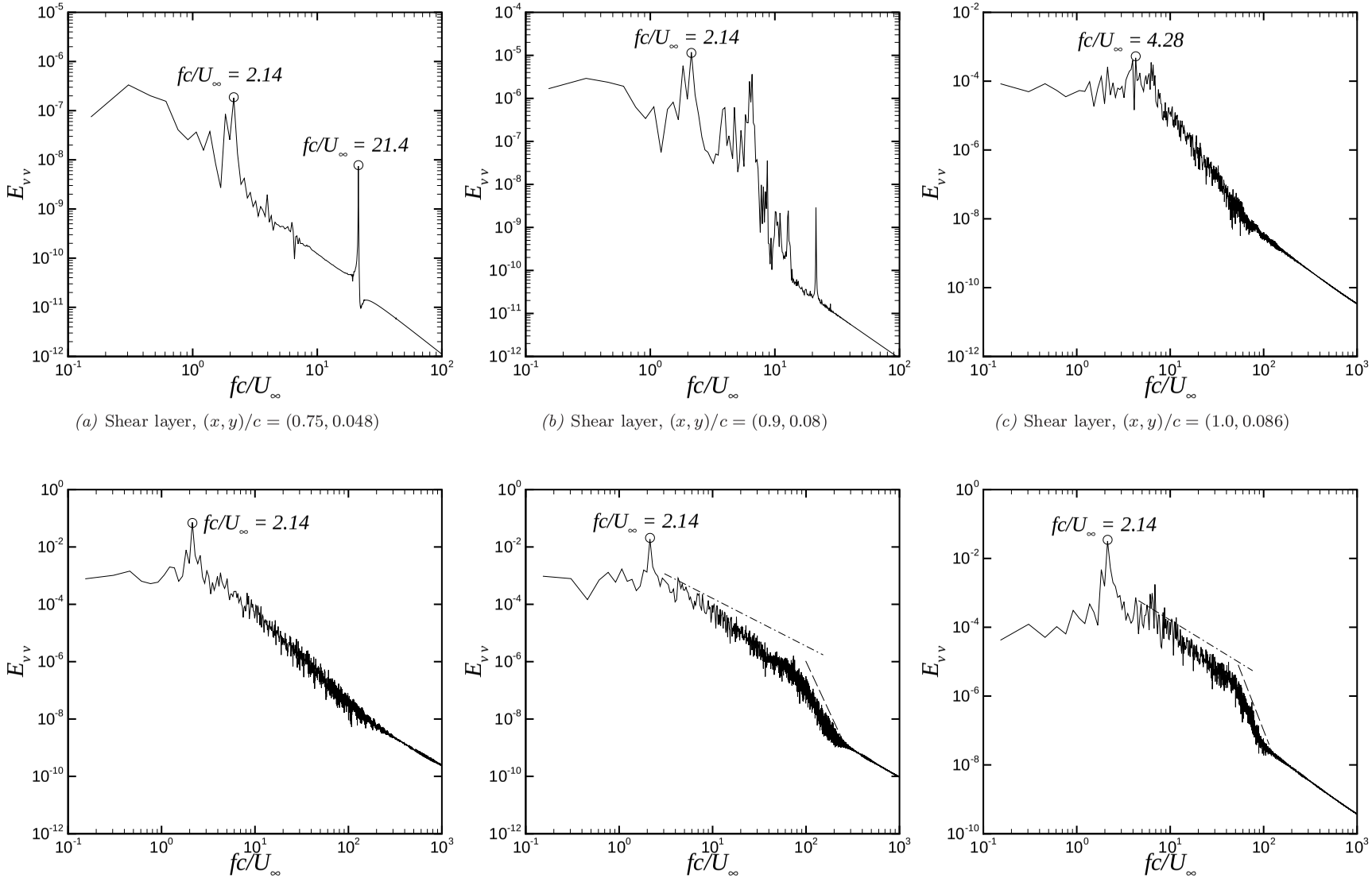

(a) Shear layer, $(x, y)/c = (0.75, 0.048)$

(b) Shear layer, $(x, y)/c = (0.9, 0.08)$

(c) Shear layer, $(x, y)/c = (1.0, 0.086)$

(d) Separated zone, $(x, y)/c = (1.07, 0.015)$

(e) Separated zone, $(x, y)/c = (1.15, 0.08)$

(f) Wake, $(x, y)/c = (1.39, -0.014)$

Figure 23. Spanwise-averaged power spectra corresponding to the temporal variations of cross-stream velocity, in the shear layer (*a*–*c*), separation zone (*d*–*e*) and wake (*f*), obtained from LES of Case 5 ($f_J = 10f^0_{lock}$) on Grid II. ——— , E_{vv}; —·— , $F^{-5/3}$; – – – , F^{-7}.

as measured from the trailing face. Thus, except for the turbulent flow in the wake, the overall spectral dynamics and the resulting lock-on states of the forced flow in the 3-D simulations are very much in line with those in the 2-D simulations.

VII. Conclusions

Large-eddy simulations were used to study the effects of three-dimensionality on the dynamics of the separated flow and its control in a flow configuration proposed by Mittal *et al*[1] for investigating active separation control using zero-net-mass-flux jets. LES of the unforced separated flow showed that the boundary layer separates earlier and the separated shear layer rolls up farther away than in 2-D simulations, resulting in an open mean separation bubble that is considerably larger than its 2-D counterpart. As in 2-D simulations, the entire system was found to be locked on to a single frequency of $f^0_{lock}c/U_\infty = 2.14$ owing to an absolute instability.[20] It was also found that the scaling laws $f^0_{sep}L_{sep}/U_\infty \approx 1$ and $f^0_{wake}W_{wake}/U_\infty \approx 0.24$, observed in the 2-D simulations, also hold in 3-D simulations. This implies that these laws have approximately the same constant of proportionality in both 2-D and 3-D simulations and so the apparent decrease in $f^0_{sep}c/U_\infty$ with increase in L_{sep} in going from 2-D to 3-D simulations.

ZNMF forcing of the above separated flow in LES was found to result in two-dimensionalization of the bulk flow. Even though, the shear layer undergoes earlier transition to turbulence due to ZNMF forcing, this accelerated laminar–turbulent transition does not play as significant a role in separation control as the large coherent structures that result from the discretization of the shear layer due to ZNMF forcing. While forcing at f^0_{lock} and $2f^0_{lock}$ reduced the size of the separation bubble significantly and reestablished pressure recovery in the aft-chord region, forcing at $4f^0_{lock}$ and $10f^0_{lock}$ was essentially ineffective, thereby confirming the exclusive effectiveness of forcing in the medium-frequency range in both 2-D and 3-D simulations. In particular, forcing at $f_J = 2f_{lock}$ generated a train of vortices close to the wall that led to regularization of the flow field and most effective separation control. Except for the well-developed turbulent flow in the wake, the overall spectral dynamics and the resulting lock-on states of the forced flow in the 3-D simulations were very much in agreement with those in the 2-D simulations.

Acknowledgments

The work presented here was supported by the U. S. Air Force Office of Scientific Research (AFOSR) under Grant F49550-05-1-0169 to RM monitored by Dr. Rhett Jefferies. RM and RBK also acknowledge support from CTR through the 2006 CTR Summer Program and the use of CTR's CDP code for the numerical simulations. The work presented here was also supported in part by a grant of computer time from the Department of Defense (DoD) High Performance Computing Modernization Program (HPCMP) at the following Major Shared Resource Centers (MSRC): US Army Research Laboratory (ARL), Aberdeen Proving Ground, MD; US Army Engineer Research and Development Center (ERDC), Vicksburg, MS.

References

[1]Mittal, R., kotapati, R. B., and Cattafesta, L. N., "Numerical Study of Resonant Interactions and Flow Control in a Canonical Separated Flow," No. 2005-1261 in AIAA Paper, 2005.

[2]Kotapati, R. B., Mittal, R., and Cattafesta, L. N., "Numerical Experiments in Synthetic Jet Based Separation Control," No. 2006-0320 in AIAA Paper, 2006.

[3]Kotapati, R. B., Mittal, R., Marxen, O., Ham, F., and You, D., "Numerical Simulations of Synthetic Jet Based Separation Control in a Canonical Separated Flow," No. 2007-1308 in AIAA Paper, 2007.

[4]Na, Y. and Moin, P., "Direct Numerical Simulation of a Separated Turbulent Boundary Layer," *J. Fluid Mech.*, Vol. 370, 1998, pp. 175–201.

[5]Schaeffler, N. W., Jenkins, L. N., and Hepner, T. E., "CASE 2: Experimental Evaluation of an Isolated Synthetic Jet in Crossflow," *Proc. NASA LaRC Workshop on CFD Validation of Synthetic Jets and Turbulent Separation Control, Williamburg, Virginia, March 29-31*, 2004.

[6]Germano, M., Piomelli, U., Moin, P., and Cabot, W. H., "A dynamic subgrid-scale eddy viscosity model," *Phys. Fluids A*, Vol. 3, 1991, pp. 1760–1765.

[7]Lilly, D. K., "A proposed modification of the Germano subgrid-scale closure method," *Phys. Fluids A*, Vol. 4, 1992, pp. 633–635.

[8]Mittal, R. and Moin, P., "Suitability of upwind-biased finite difference schemes for large-eddy simulation of turbulent flows," *AIAA J.*, Vol. 35, 1997, pp. 1415–1417.

[9]Harlow, F. H. and Welch, J. E., "Numerical calculation of time-dependent viscous incompressible flow of fluid with free

surface," *Phys. Fluids*, Vol. 8, 1965, pp. 2182–2189.

[10]Ham, F., Mattson, K., and Iaccarino, G., "Accurate and stable finite volume operators for unstructured flow solvers," Tech. rep., Annual Research Briefs 2006, Center for Turbulence Research, Stanford University, 2006.

[11]Kim, D. and Choi, H., "A second-Order Time-Accurate Finite Volume Method for Unsteady Incompressible Flow on Hybrid Unstructured Grids," *J. Comp. Phys.*, Vol. 162, 2000, pp. 411–428.

[12]Mahesh, K., Constantinescu, G., and Moin, P., "A Numerical Method for Large Eddy Simulations in Complex Geometries," *J. Comp. Phys.*, Vol. 197, 2004, pp. 215–240.

[13]Haworth, D. C. and Jansen, K., "Large-eddy simulation on unstructured deforming meshes: towards reciprocating IC engines," *Computers and Fluids*, Vol. 29, 2000, pp. 493–524.

[14]Ham, F. and Iaccarino, G., "Energy Conservation in Collocated Discretization Schemes on Unstructured Meshes," Tech. rep., Annual Research Briefs 2004, Center for Turbulence Research, Stanford University, 2004.

[15]Karypis, G., Schlogel, K., and Kumar, V., "ParMETIS: Parallel graph partitionaing and sparse matrix ordering library - Version 3.1," Tech. rep., University of Minnesota, Department of Computer Science and Engineering, Minnesota, MN 55455, 2003.

[16]Mittal, R. and Balachandar, S., "Effect of three-dimensionality on the lift and drag of nominally two-dimensional cylinders," *Phys. Fluids*, Vol. 7, 1995, pp. 1841–1865.

[17]Tennekes, H. and Lumley, J. L., *A First Course in Turbulence*, The MIT Press, 1st ed., 1972.

[18]Hinze, J. O., *Turbulence*, McGraw–Hill, 2nd ed., 1975.

[19]Taylor, G. I., "The spectrum of turbulence," *Proc. R. Soc. London Ser.*, Vol. A164, 1938, pp. 476–490.

[20]Ho, C. M. and Huerre, P., "Perturbed Free Shear Layers," *Annu. Rev. Fluid Mech.*, Vol. 16, 1984, pp. 365–424.

[21]Seifert, A., Eliahu, S., and Greenblatt, D., "Use of Piezoelectric Actuators for Airfoil Separation Control," *AIAA J.*, Vol. 36, 1998, pp. 1535–1537.

[22]Marxen, O., *Numerical Studies of Physical Effects Related to the Controlled Transition Process in Laminar Separation Bubbles*, Ph.D. thesis, Universität Stuttgart, 2005.